Session MT-2

Modeling and Testing(2)

Chemo-thermo-viscoelastic Behavior of Underfill Materials during Curing Process
(*Invited*)
Sung YI, Kerm Sin CHIAN, Nanyang Technological University, Singapore

Electrical Characteristics of Single and Coupled Stripline on Meshed Ground Plane in High-Speed Package
Heeseok LEE, Joungho KIM, Korea Advanced Institute of Science and Technology, Korea

An Experimental Study on the Package Stress in Plastic Encapsulated IC(Integrated Circuit)
Minju LEE, ASE Korea Inc., Korea
Won-Gu JOO, Yonsei University

Adaptation of neural network and application of digital ultrasonic image processing for the pattern recognition of defects in Semiconductor

Jae-Yeol Kim, Hyun-Jo Jeong, Hun-Cho Kim, Chang-Hyun Kim

Chemo-thermo-viscoelastic Behavior of Underfill Materials During Curing Process

Sung Yi*and Kerm Sin Chian
School of Mechanical and Production Engineering
Nanyang Technological University
Singapore 693798, Republic of Singapore

ABSTRACT

The mechanical properties of thermosetting under-fill materials strongly depend on the curing process itself and, hence, it is important to understand the effects of temperature distributions and degree of cure on the mechanical behavior of the underfill. Moreover, the understanding of rheological changes during the curing process is essential for the manufacturing process optimization . In this paper, the chemo-thermo-rheological behavior of the underfill material during the cure process is presented. These experiments reveal the material properties dependent on temperature and degree of cure. Cure kinetics for underfill materials are determined. In addition, constitutive relations of underfill materials during curing process are presented using mechanical models with time temperature and cure dependent parameters.

Keywords: cure process, chemo-thermo-rheological behavior of underfill materials, constitutive relations of underfill materials during curing process, flip-chips

INTRODUCTION

Underfill materials have been used to protect the solder joint from being damaged during thermal cycling. It

To whom correspondence should be addressed. Tel: (65) 790-6239, Fax: (65) 791-1859, Email: msyi@ntu.edu.sg

is reported that that the presence of underfill layer at the flip chip assembly enhances the reliability of the assembly by more than ten folds [1-2]. Underfilling process involves dispensing a controlled amount of silica filled epoxy into a gap between flip chips and substrates. The underfill material is dispensed along a line adjacent to the edge of the die and is allowed to flow into the gap between the die passivation layer and the substrate surface under capillary action. It is critical that the gap is completely filled with the underfill material as the life of the flip chip assembly is dependent on it. In our previous study[?], the underfill dispensing process has been studied using statistical tools. It is very important to understand the chemo-thermo-rheological behavior of the underfill material in order to achieve the good flow performance and improve the reliability of products.

During cure, underfill materials are subject to chemical and material changes, thermal gradients and to creep and relaxation. During the curing process, the underfill is a liquid-like material at the beginning of the process and has low molecular weight. As the crosslinking reaction proceeds, the molecular weight and viscosity increase. In this region, the resin is a viscoelastic fluid with mechanical properties which change during the process. The crosslinking reaction depends on temperature, resin type, curing agent, etc. The molecular weight increases further and then reaches the gel point, which is defined as the instant at which the average molecular weight or viscosity diverges to infin-

ity. At this gel point, phase transition occurs to a viscoelastic solid and then the equilibrium modulus of the resin grows with higher crosslink density until the reaction stops. The heat required for polymerization in resins causes chemical changes in the molecular structure. Resins have crosslinked structures with covalent bonds between molecules and cross linking reactions are dependent on applied temperatures. Additionally, internal heat is also generated by chemical reactions. During the cure process, the material structure actually undergoes a continuous phase transformation from a liquid to a viscoelastic solid and increasing the number and length of the polymer chains leads to one tremendous molecule, namely, a crosslinked or network polymer.

The mechanical properties of thermosetting resins strongly depend on the curing process itself and, hence, it is important to understand the effects of temperature distributions and degree of cure on the mechanical behavior of underfill materials. It is, therefore, required to accurately develop analytical models which properly describe the rheological behavior of thermosetting resins during the cure process. In the authors' previous studies (Yi *et al.* 1994a, b, 1995a, b, c, 1996), constitutive relations for thermosetting resins have been developed which represent isotropic/anisotropic nonhomogeneous viscoelastic chemo-rheological thermal and material behavior of thermosetting materials during the manufacturing process. These formulations are based on the construction of mathematical relations achieved with the help of mechanical models possessing time, temperature and cure dependent material property parameters. Thus, material behavior of thermosetting resins during curing processes, including phase changes, is describable by the Yi-Hilton models (YHM), which can be independently associated with any appropriate cure kinetics.

In the present study, chemo-thermo-rheological responses of underfill materials are experimentally characterized during curing processes. The dynamic mechanical experiments on underfill materials are performed. Cure kinetics for underfill materials are determined. In addition, constitutive relations of underfill materials during curing process are presented using mechanical models with time temperature and cure dependent

parameters. These results are of importance to the researcher as well as to designers of underfilling and service processes.

ANALYSIS

Degree of Cure and Cure Kinetics

The kinetics of the curing thermosetting resins have been studied by many researchers. The heat of reaction H up to time t can be calculated by [8]

$$H = \int_0^t \left(\frac{dQ}{ds}\right) ds \qquad (1)$$

where dQ/ds is the rate of heat generation.

Dynamic measurements of glass transition temperatures and heats of reaction of the resin as a function of time and temperature yield information relating to cure and consequently curing kinetics can be obtained. The degree of cure α is defined as

$$\alpha = \frac{H}{H_T} \qquad (2)$$

with

$$H_T = \int_0^{t_f} \left(\frac{dQ}{ds}\right) ds \qquad (3)$$

where t_f is the time required to complete the reaction and H_T is the amount of heat generated during dynamic scanning until the completion of the chemical reactions. The rate of cure is a parameter proportional to the rate of heat release at an isothermal temperature T_I which can be defined as

$$\frac{d\alpha}{dt} = \frac{1}{H_T} \left(\frac{dQ}{dt}\right)_{T_I} \qquad (4)$$

where $(dQ/dt)_{T_I}$ is the rate of heat generation and is provided by the measurements.

Based on empirical rate laws, a variety of kinetic models are developed in order to describe the curing process of thermosetting systems. Using a modified Arrhenius type equation, the rate of degree of cure can be expressed as a function of degree of cure itself. Two empirical schemes, nth order and bi-nodal models, are widely

used for modeling cure kinetics for thermosetting materials. The nth order kinetics can be expressed as

$$\frac{d\alpha}{dt} = k_0(1-\alpha)^n \qquad (5)$$

Kamal *et al.*[9] proposed the following curing kinetic model

$$\frac{d\alpha}{dt} = (k_1 + k_2\alpha^m) \cdot (1-\alpha)^n \qquad (6)$$

where k_0, k_1 and k_2 are rate constants, which depend on temperature, and m and n are constants. In the above, the rate constants k_0, k_1 and k_2 are usually assumed to be of the Arrhenius form. Eq. (6) requires that the initial reaction rate is maximum at the beginning of cure. However, in epoxy cure, this is not the case. Therefore, Eq. (7) which allows an induction period during the reaction period is frequently utilized in modeling cure of epoxy resin.

Constitutive Relationships for Resins

The constitutive relations for thermosetting resins during curing process have been modeled by mechanical models with temperature and cure dependent parameters in Refs. 4-5. In our previous study, the spring and viscous damping parameters depend on temperature and degree of cure. If one assumes that the resin is isotropic, then the stress tensor σ_{ij} can be decomposed into dilatational one (volumetric one) and deviatoric one and that can be stated in the Cartesian coordinates.

$$\sigma_{ij} = \frac{1}{3}\sigma_{kk} \cdot \delta_{ij} + \tau_{ij} \qquad (7)$$

$$\sigma_{kk} = \sigma_{11} + \sigma_{22} + \sigma_{33} \qquad (8)$$

where $i,j = 1,2,3$ and δ_{ij} is the Kronecker delta. Similarly, the strain tensor ϵ_{ij} can also be defined as

$$\epsilon_{ij} = \frac{1}{3}\epsilon_{kk} \cdot \delta_{ij} + \gamma_{ij} \qquad (9)$$

$$\epsilon_{kk} = \epsilon_{11} + \epsilon_{22} + \epsilon_{33} \qquad (10)$$

where ϵ_{kk} and γ_{ij} are the dilatational strain and the deviatoric strain tensors respectively.

The mechanical models are used to visualize and understand rheological behaviors of thermosetting polymers during cure. In the Kelvin model, the stress-strain relations for the mechanical components are

$$\tau_{ij}^{(s)}(\mathbf{x},t) = E^s\gamma_{ij}(\mathbf{x},t), \qquad \frac{\partial\gamma_{ij}(\mathbf{x},t)}{\partial t} = \frac{\tau_{ij}^{(d)}(\mathbf{x},t)}{\eta^s} \quad (11)$$

and

$$\tau_{ij} = \tau_{ij}^{(s)} + \tau_{ij}^{(d)} \qquad (12)$$

where (s) and (d) denote the spring and the dashpot respectively, τ_{ij} are the stresses for the Kelvin element, $\gamma_{ij}^{(s)}$ and $\gamma_{ij}^{(d)}$ are the associated strains for the spring and the damper with shear modulus E^s and coefficient of viscosity η^s.

Thermosetting resins are polymerized by applying temperatures and pressures for some lengths of time. The heat required for polymerization in resins causes chemical changes in the molecular structure. Resins have crosslinked structures with covalent bonds between molecules and cross linking reactions are dependent on applied temperatures. Additionally, internal heat is also generated by chemical reactions. During the cure process, the material structure actually undergoes a continuous phase transformation from a liquid to a viscoelastic solid and increasing the number and length of the polymer chains leads to one tremendous molecule, namely, a crosslinked or network polymer. The volume shrinkage of thermosetting resins during cure also occurs mainly due to the chemical reaction and temperature change. Therefore, the constitutive relations for thermosetting resins during curing process can be modeled by mechanical models with temperature and cure dependent parameters. The spring and viscous damping parameters depend on temperature and degree of cure in the following manner

$$E^s = E^s(T,\alpha), \qquad \eta^s = \eta^s(T,\alpha) \qquad (13)$$

In the above, temperature T is a function of time t, degree of cure α is a function of time t as well as tempera-

ture. In the following section, temperature and cure dependency of these material parameters are discussed in detail. By using the generalized Kelvin model, the total deviatoric and dilatational deformations of the polymer resins can be described as

$$2\gamma_{ij}(t) = \frac{\tau_{ij}(t)}{E_0^s} + \int_{0^-}^t \frac{\tau_{ij}(s)}{\eta_{m+1}^s} ds$$

$$+ \sum_{p=1}^m \int_{0^-}^t \exp[-(\zeta_p^s - \zeta_p^{s'})]\frac{\tau_{ij}(s)}{\eta_p^s} ds \qquad (14)$$

$$3[\epsilon_{kk}(t) - 3\epsilon^*(t)] = \frac{\sigma_{kk}(t)}{E_0^v} + \int_{0^-}^t \frac{\sigma_{kk}(s)}{\eta_{m+1}^v} ds$$

$$+ \sum_{p=1}^m \int_{0^-}^t \exp[-(\zeta_p^v - \zeta_p^{v'})]\frac{\sigma_{kk}(s)}{\eta_p^v} ds \qquad (15)$$

where m is the number of Kelvin elements, superscripts s and v denote deviatoric and volumetric respectively. ϵ^* is chemo-thermally induced strain in the stress-free state which are related to the thermal expansion coefficients b_T and chemical shrinkage coefficient b_α:

$$\epsilon^* = \epsilon^{th} + \epsilon^{ch} = \int_{T^*}^T b_T(s)ds + \int_{\alpha^*}^\alpha b_\alpha(s)ds \qquad (16)$$

In the above, ϵ^{th} and ϵ^{ch} are volumetic thermal strains and chemical shrinkage strains respectively, and T^* and α^* are stress-free reference temperature and cure. The ζ_p^s and ζ_p^v functions are

$$\zeta_p^s(t,T,\alpha) = \int_0^t \frac{E_p^s(T,\alpha)}{\eta_p^s(T,\alpha)} ds = \int_0^t \frac{1}{\lambda_p^s(T,\alpha)} ds \qquad (17)$$

$$\zeta_p^v(t,T,\alpha) = \int_0^t \frac{E_p^v(T,\alpha)}{\eta_p^v(T,\alpha)} ds = \int_0^t \frac{1}{\lambda_p^v(T,\alpha)} ds \qquad (18)$$

where λ_p^s and λ_p^v are temperature and cure dependent retardation times. Similarly, the deviatoric and dilatational stress-strain relationships for the generalized Maxwell body can be expressed as

$$\frac{\tau_{ij}(t)}{2} = \widehat{E}_0^s\gamma_{ij}(t) + \widehat{\eta}_{m+1}^s\frac{\partial\gamma_{ij}}{\partial t} + \sum_{p=1}^m \int_{0^-}^t \widehat{E}_p^s$$

$$\cdot\exp[-(\zeta_p^s - \zeta_p^{s'})]\frac{\partial\gamma_{ij}}{\partial s} ds \qquad (19)$$

$$\frac{\sigma_{kk}(t)}{3} = \widehat{E}_0^v\epsilon_{kk}(t) + \widehat{\eta}_{m+1}^v\frac{\partial\epsilon_{kk}}{\partial t} + \sum_{p=1}^m \int_{0^-}^t \widehat{E}_p^v$$

$$\cdot\exp[-(\widehat{\zeta}_p^v - \widehat{\zeta}_p^{v'})]\frac{\partial(\epsilon_{kk} - 3\epsilon^*)}{\partial s} ds \qquad (20)$$

where

$$\widehat{\zeta}_p^s(t,T,\alpha) = \int_0^t \frac{\widehat{E}_p^s(T,\alpha)}{\widehat{\eta}_p^s(T,\alpha)} ds = \int_0^t \frac{1}{\widehat{\lambda}_p^s(T,\alpha)} ds \qquad (21)$$

$$\widehat{\zeta}_p^v(t,T,\alpha) = \int_0^t \frac{\widehat{E}_p^v(T,\alpha)}{\widehat{\eta}_p^v(T,\alpha)} ds = \int_0^t \frac{1}{\widehat{\lambda}_p^v(T,\alpha)} ds \qquad (22)$$

and ^ denotes Maxwell body and $\widehat{\lambda}_p^s$ and $\widehat{\lambda}_p^v$ are temperature and cure dependent relaxation times.

Mechanical models and integral equations are equivalent. The constitutive equations may also be written as hereditary integrals. The coefficients in those equations represent the material properties and, therefore, in this present study, those coefficients are functions of time, temperature, and cure. The stress-strain relations in hereditary integral form are

$$\tau_{ij}(t) = 2\int_{0^-}^t G[t,s,T,\alpha,]\frac{\partial\gamma_{ij}(s)}{\partial s} ds \qquad (23)$$

$$\sigma_{kk}(t) = 3\int_{0^-}^t K[t,s,T,\alpha]\frac{\partial}{\partial s}[\epsilon_{kk}(s) - 3\epsilon^*(s)] ds \qquad (24)$$

or

$$\gamma_{ij}(t) = \frac{1}{2}\int_{0^-}^t J_s[t,s,T,\alpha]\frac{\partial\tau_{ij}(s)}{\partial s} ds \qquad (25)$$

$$\epsilon_{kk}(t) - 3\epsilon^*(t) = \frac{1}{3}\int_{0^-}^t J_v[t,s,T,\alpha]\frac{\partial\sigma_{kk}(s)}{\partial s} ds \qquad (26)$$

RESULTS AND DISCUSSION

In this study, the chemo-thermo-rhelogical properties of underfill materials has been determined during

isothermal cure. The important effects of cure on the viscosity of the underfill can therefore determined if sufficient analysis is carried out using suitable kinetic models to obtain the maximum cure reaction of the underfill. Differential scanning calorimeters and rheometers are used to determine heats of reaction and complex dynamic viscosities of underfill materials during the curing process. Typically 5±0.01mg of the underfill was weighed accurately and sealed in hermetic aluminium test pans and sealed before tested in the DSC. Isothermal studies were conducted at 110 °C, 120 °C and 125 °C. TA instrument model 2920 Differential Scanning Calorimeter (DSC) was used to monitor the curing rate and the degree of cure of the underfill materials as a function of time. The underfill was heated from room temperature to 250 °C at a heating rate of 5 and 10 °C/min using DSC and the heat flow was converted to degree of conversion. Figure 2 shows that conversion as a function of temperature. The cure kinetics for the underfill materl can be expressed using the autocatalytic empirical model as

$$\frac{d\alpha}{dt} = k_2 \alpha^m \cdot (1-\alpha)^n \qquad (27)$$

For the underfill, the reaction order for reacted functional group m is 0.654 ± 0.018 and n is 0.942 ± 0.031. The activation energy (70.6 ± 6.4 kJ/mole).

Rheometer RS-150 from Haake was used to determine the viscosity of the underfill material as a function of temperature. The heating rate for this experiment is maintained as 5 °C/min when the material is heated from the room temperature to 150 °C under oscillatory mode. The frequency was maintained at 1Hz with a shear deformation of 5thermosetting resins during the cure process. It is assumed that the modulus of the underfill is negligible before the gelation. The viscosity that depends on temperature and the degree of cure can be described as

$$\eta(\alpha, T) = A \exp\left[\frac{-C_1(T-T_g)}{C_2 + (T-T_g)}\right]\left(\frac{\alpha_g}{\alpha_g - \alpha}\right)^{C_3 + C_4\alpha} \qquad (28)$$

where A, C_1, C_2, C_3, C_4 are curve-fitting coefficients, and T_g, α_g are glass transition temperature of unreacted epoxy system and conversion at gelation point respectively. The viscosity as a function of temperature was determined using rheometer and the curvefitted results were given in Table 1.

The degree of cure at various temperature conditions is plotted in Fig. 1. The results shows that it takes a longer time to achieve full cure at lower curing temperature. The excellent agreement was obtained between the experimental results and the model. Fig. 2 shows that the conversion is not influenced by the heating rate. The viscosity versus the conversion is illustrated in Fig. 3. The viscosity increases dramatically with increasing the degree of cure. As shown in Fig. 4, the rate of cure increase overcomes the temperature induced softening effects so that the increase of the viscosity is observed. At the isothermal condition, the viscosity versus time is plotted in Fig. 5.

CONCLUSIONS

The chemo-rheological behavior of the underfill during curing process have been characterized using the DSC and the rheometer. The results show that the mechanical properties of the underfill strongly depend on the temperature and curing process itself.

REFERENCES

1. M. K. Schwiebert and W. H. Leong (1996) "Underfill flow as Viscous Flow Between Parallel Plates Driven by Capillary Action", *IEEE Transaction of components- Part C*, Vol.19, No 2, pp.133-137.

2. T.Y. Wu, Y. Tsukada and W. T. Chen, (1996). Materials and mechanics issues in flip chip organic packaging. *Electronics Components and Technology Conference*, pp.524-534.

3. Y. C. Chia, S. H. Lim, K. S. Chian, S. Yi and W. T. Chen, "An Optimization Study of Underfill Dispensing Process", *Interpack 99*, June 1999.

4. S. Yi and H.H. Hilton (1995a) "Constitutive relations for thermosetting resins during curing processes," *Proceedings 36th AIAA/ASME/ASCE/AHS/ASC Structures, Structural Dynamics and Materials Conference, AIAA Paper 95-1428.*

5.   S. Yi, H. H. Hilton and M. F. Ahmad, (1997) "Finite Element Approach for Cure Simulation of Thermosetting Matrix Composites", *Computers and Structures*, UK, Vol. 64, No. 1-4, pp. 383-388.

6. S. Yi, H. H. Hilton and M. F. Ahmad, (1998) "Cure Cycle Simulations of Composites with Temperature and Cure Dependent Anisotropic Viscoelastic Properties and Stochastic Delaminations", *Mechanics of Composite Materials Structures*, Vol. 5, pp.81-101.

7.   S. Yi, H. H. Hilton and M. Fouad Ahmad (1995c) "Curing process induced viscoelastic residual stresses in polymer matrix laminated composites," *Proceedings Symposium on Design and Manufacture of Composites, 1995 Winter Annual Meeting of ASME* **MID-69-1**:65-76.

8. Prime, R. B., "Differential Scanning Calorimetry of the Epoxy Cure Reaction," *Polymer Engineering and Science*, Vol. 13, 1973, pp. 365-371.

9.   M. R. Kamal and S. Sourour, (1973),"Kinetics and Thermal Characterization of Thermoset Cure," *Polymer and Engineering Sience*, Vol. 13, pp. 59.
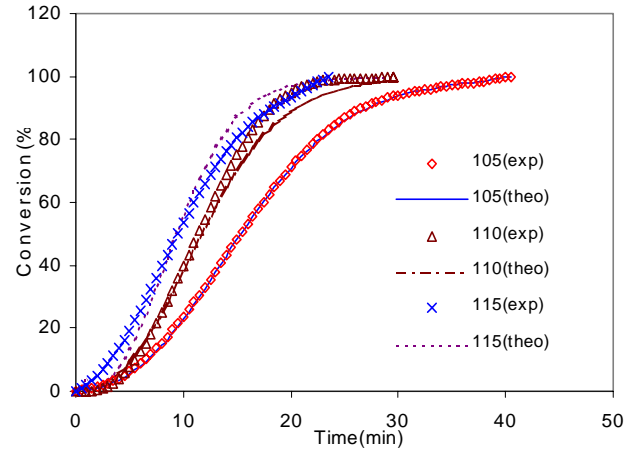
Figure 1: Degree of cure versus time

Table 1: Curve-fitting Coefficients

Parameters	A	C_1	C_2	C_3
value	9174.548	22.2515	141.4596	1.15539

Parameters	C_4	T_g	α_g
value	0.11	-52.26	55.45
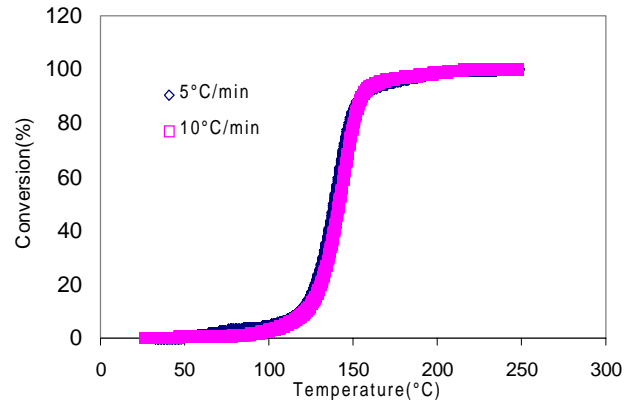
Figure 2: Conversion versus temperature
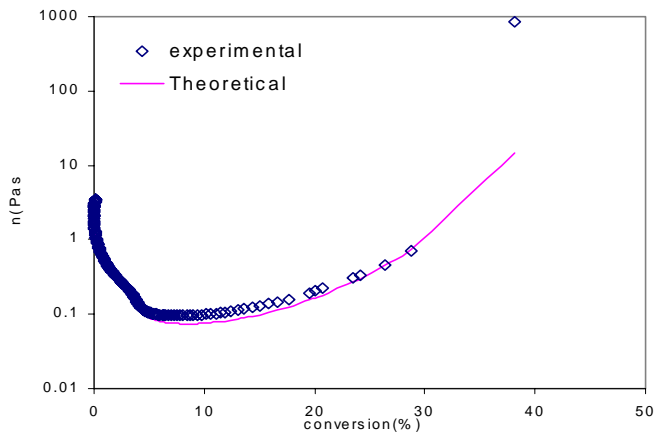
Figure 3: Viscosity versus Degree of Cure
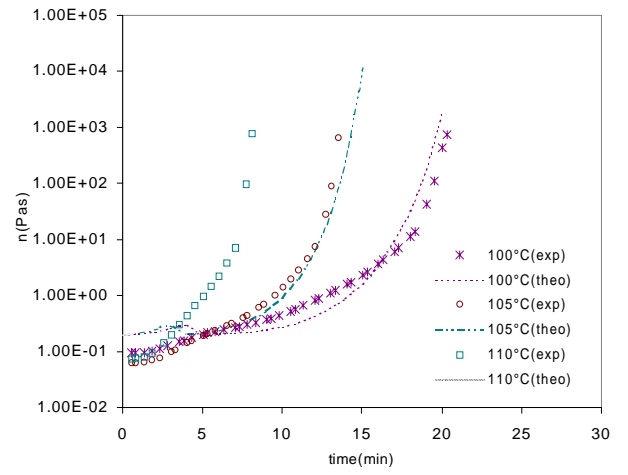
Figure 5: Isothermal Results.
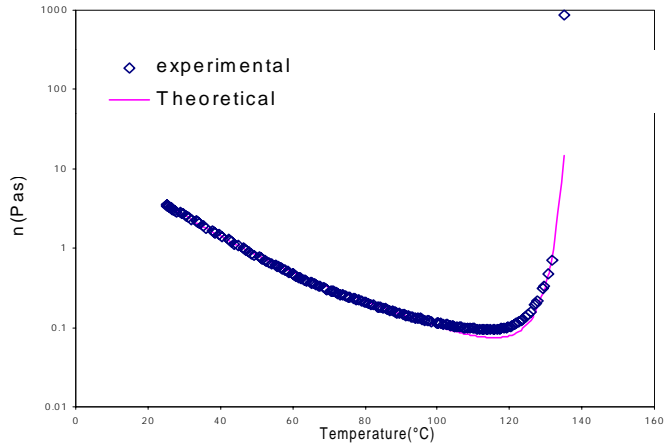
Figure 4: Viscosity versus temperature

7

An Experimental Study on the Package Stress in Plastic Encapsulated IC(Integrated Circuit)

Minju Lee
Advanced Semiconductor Engineering, Inc., Korea
494, Munbal-Ri, Kyoha-Myon, Paju-Si, Kyunggi-Do, 413-830 Korea
e-mail: mjlee@asekr.com   phone: 82-31-940-0569   fax: 82-31-940-0629

Won-Gu, Joo
Department of Mechanical Engineering
Yonsei University, Seoul, Korea
e-mail: joo_wg@yonsei.ac.kr   phone:82-2-2123-2815   fax:82-2-2123-2159

Abstract

Transfer molding is the primary process for the IC (Integrated Circuit) encapsulation with EMC (Epoxy Molding Compound) and also the most extensive method for plastic packaging. Plastic encapsulated package offers many advantages over their other counterparts such as low cost, lightweight, and ready availability that accounted for approximately 98% of IC packages produced within the microelectronics industry. The recent trends in plastic packaging becomes thinner and smaller where drawbacks are more serious to package stress from transfer molding process. It is for the reason the needs of thorough understanding of package stress are becoming greater. In this paper, flow-induced package stress is experimentally visualized to analyze time-dependence flow characteristics of EMC by employing different geometrical gate design parameters. Also, EMC with different material properties are evaluated to quantify influence on package stress as interfacial adhesion, warpage, voiding, wire sweep, and penetration rate. In addition, screening DOE (Design of Experiment) is performed to identify main process parameters, as well as optimum window of critical parameters is defined by RSM (Response Surface Methodology).

1. Introduction

Advanced electronics based on plastic packaging is rapidly growing technology in semiconductor industry. As the plastic package becomes smaller and smaller in size, otherwise, low cost with adequate package reliability is continuously required in the recent market. [1]

In general, the function of plastic encapsulation is to protect the chip by sealing the package from environmental hazards such as heat, humidity and vibration. For the plastic encapsulation technology, transfer molding is primary process for microelectronic encapsulation with epoxy molding compound (EMC). In the process a heated EMC is forced, under the motion of a plunger, to flow through runners and gates into heated cavity where the substrate or leadframe are pre-placed [2]. It has defined that there are three major contributors determining the characteristics of package reliability from transfer molding process. For critical factors to be considered in transfer molding process, it can be summarized that mold design, material properties of EMC, and molding process condition. [3]

As the previous studies, A. Brent Strong [4] presents general considerations for mold design parameters, especially in geometrical design parameters for runner and gate. To enhance reliability of plastic package, Wei H. Koh, Bevely H. Tai and Elizbeth A. Kolawa [5] studied low stress encapsulants for reduced failures in plastic packages. Since package reliability required in transfer molding process, corresponds to mold design, material properties of EMC, and molding process condition as mentioned above, there is necessity to study for overall transfer molding process in systematical manner.

The purpose of this study is to experimentally visualize flow front of EMC by employing different geometrical gate design, and to qualitatively analyze flow-induced package stress resulting from EMC flow patterns. Secondly, EMCs with different material properties are evaluated to quantify influence on package reliability. Finally, based on the selected gate design and EMC defined, parameters optimization is conducted to improve package molding quality by using statistical methods.

2. Experimental Study

2.1 Geometrical gate design parameters

In transfer molding process, the pressure is the highest at the transfer pot and decrease to atmospheric pressure at the advancing flow fronts. The pressure gradient is nonlinear because of the changes in volumetric flow rate as EMC is diverted into the mold cavity, and the temperature, viscosity and velocity gradients that are inherent to the transfer molding process. The gate that is closer to the transfer pot experiences the higher pressure.

It is well known fact that the EMC flow in the cavity determines the extent of the flow-induced stresses that are imposed on the substrate and wire bonds, thereby affecting the package reliability. Understanding and quantifying the pressure drop through the gate is necessary for controlling the mold-filling behavior since the flow of the EMC through the gate determines the mold filling behavior to a large extent. Flow through the gate also has an influence on the temperatures and viscosity of the EMC as it contacts the substrate.

To control EMC flow in the cavity and reduce flow-induced package stress, Louis T. Mazione [6] quantified the

pressure drop versus volumetric flow rate through the gates with 3 geometrical parameters such as width, depth and angle.

In this paper, geometrical gate design parameters – Length (L), Depth (D), Angle (A) – are considered to visualize EMC flow fronts in the cavity using 3 colored EMC, and analyzed those effects to define level of flow-induced package stress by experimental approach. To identify time-dependence flow characteristics in the cavity, 3 colored EMC that has $30 \sim 120$ (poise) of viscosity, 130 ± 30 (cm) of spiral flow at 175 (° C), has been used for experiment and are finally observed those flow achievement in the cavity per every 1 second since when plunger begin to move up. Figure 1-2 shows 3 colored EMC with 4 different gate specimens.

Figure 1. 3 colored EMC specimen

Based on L = 38 mm, D = 1 mm, and A = 58° as geometrical gate design parameters, 1/2 scales of gate parameters are considered. Table 1 shows scaled gate specimens with molding condition for experiment.
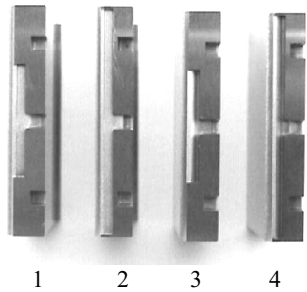
Figure 2 Gate specimens having different geometrical gate parameters

Table 1 Experimental molding condition with scaled gate parameters

Specimen (#)	Length (mm)	Depth (mm)	Angle (°)	Molding Parameter Condition	
1	0.5L	0.5D	1A	Clamp force (KN)	250
2	1L	0.5D	0.5A	Transfer pressure (bar)	25
3	0.5L	1D	0.5A	Mold cavity temperature (°C)	175
4	1L	1D	1A	Transfer speed (mm/s)	7

From the 4 different gates application, time-dependence EMC flow in the cavity is measured by every second for 3 seconds. Under the given molding condition, flow

achievement per each gate specimen is resulted in as is shown in Figure 3.

1) "0.5L-0.5D-1A" case
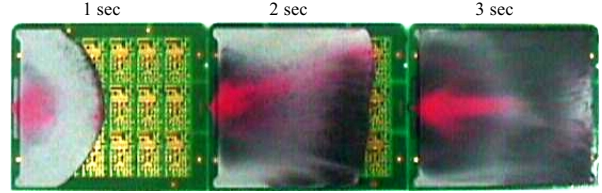
2) "1L-0.5D-0.5A" case
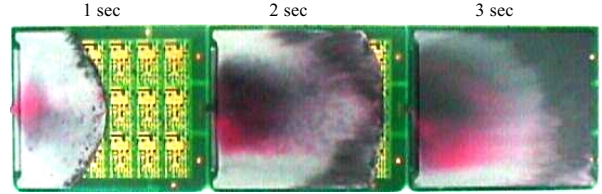
3) "0.5L-1D-0.5A" case
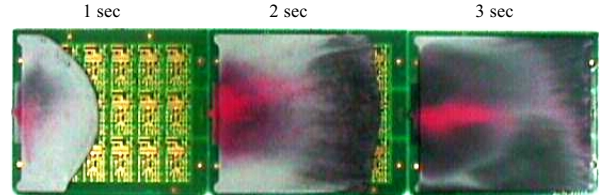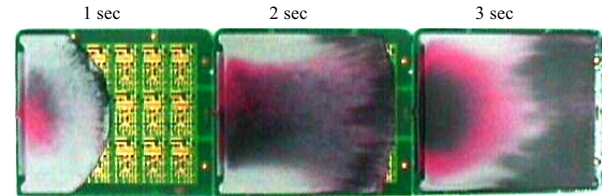

4) "1L-1D-1A" case

Figure 3. Melt front achievement of EMC

Stress concentration derives from poor adhesion along the EMC interfaces with the semiconductor chips and the substrate. With complete adhesion between the EMC and the substrates or chips, there is less stress concentration at the plastic package and thereby minimum opportunity of package failure. To identify delamination, and EMC concentration level from 4 scaled gate specimens, Sonic Acoustic Microscope (SAM) and Scanning Electron Microscope (SEM) are performed. From both C-SAM and SEM analysis shown in Figure 4, samples from "1L-1D-1A" scale gate specimen shows better package integrity and EMC concentration than samples from other scaled gates does.
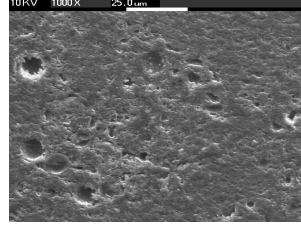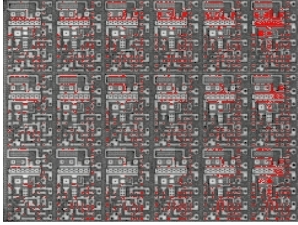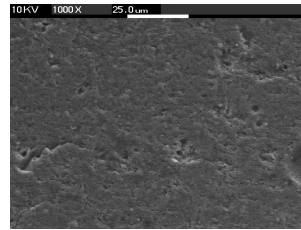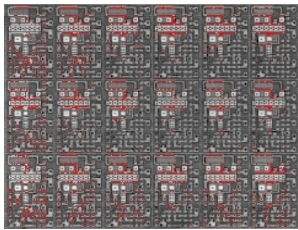
1) "0.5L-0.5D-1A" scale
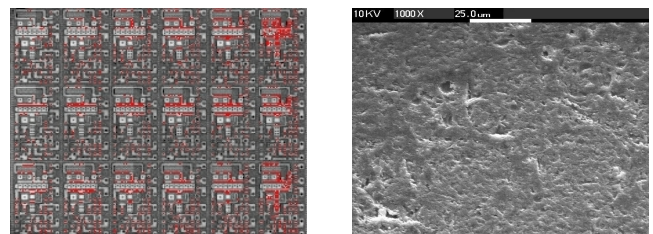
2) "1L-0.5D-0.5A" scale
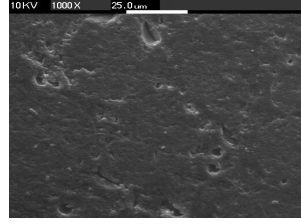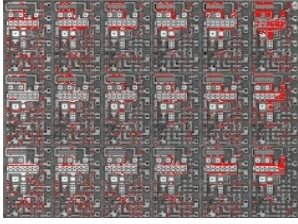
3) "0.5L-1D-0.5A" scale

4) "1L-1D-1A" scale

| (a) C-SAM micrographs for delamination (with 50MHz) | (b) SEM micrographs for EMC concentration (1000X) |

Figure 4 Delamination and EMC concentration level

2.2 Evaluation of Epoxy Molding Compound

EMC is the most important polymer material used in plastic packaging of microelectronic device and it provides mechanical, heat and moisture resistant properties that protect the device from the environmental hazards. By far, EMC is the most dominant material used because the low initial viscosity of this thermosetting material allows it to flow over the delicate substrate and wire bonds without causing significant deformation. Since EMC consists of various components such as epoxy resin, hardener, catalyst, filler and etc., this is the reason for necessity of thorough understanding of EMC behavior as one of major factors determining package reliability. To identify the potent EMC in terms of package reliability, 3 different EMCs - HC100X2, EME7725S, MG47F - with different material properties, are evaluated how EMC influences on package reliability, such as warpage of package, voiding, wire sweep, penetration rate of fluorescent material into interface between EMC and substrate. Material property with molding condition for EMC evaluation is summarized in Table 2.

Table 2 Material properties of 3 EMCs and molding condition

Application	Unit	HC100X2	EME7725S	MG47F	Molding Parameter Condition	
Spiral Flow	Cm	140	115		Clamp force (KN)	250
Gelation Time	sec	25	34			
Viscosity	Pa-s	6	120		Transfer pressure (bar)	25
CTE Alpha-1	ppm/C	7	10	14		
CTE Alpha-2	ppm/C	30	33		Mold cavity temperature (ºC)	175
T_g	ºC	160	160	150	Transfer speed (mm/s)	7
Water	85C/85% RH for 168hrs	0.31%				

Package warpage

Using 3 EMCs as described in Table 2, 10 substrates are molded under the given molding condition, and then Post Mold Cure (PMC) is conducted at 175± 5 (℃) during 90 minutes. Warpage of package is measured before and after PMC, and compared to it as shown in Figure 5. As the facility of warpage measurement, Mitutoyo PH-3500 is used. From the Figure 5, HC100X2 shows warpage level decrease to 0.8636 mm, and then again MG47F results in almost no change of warpage level before and after PMC.
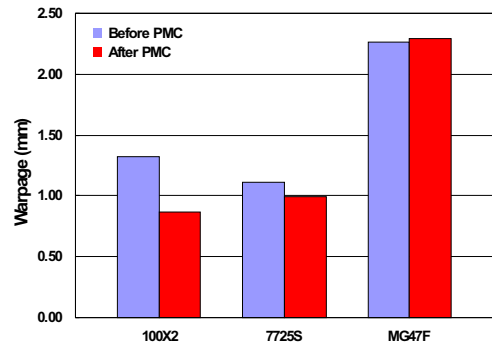

Figure 5 Package Warpage before and after PMC

Package voiding

Over 0.5 mm in diameter of package voiding is quantified by visual inspection after package singualtion. Voiding rate (unit %) of package shows 7.4% for HC100X2, 11.1% for 7725S, and 20.4% for MG47F as shown in Figure 6.
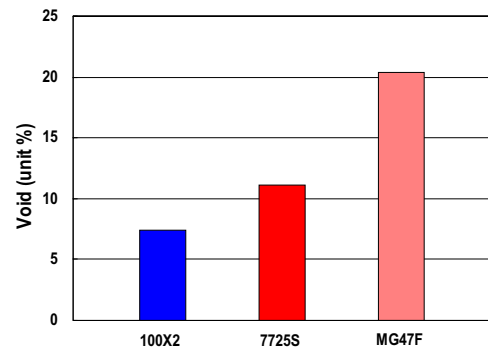

Figure 6 Package voiding rate (unit %)

Wire Sweep

As the wire sweep criteria, level of wire sweep is divided by sweeped wire (%), such as under 5%, 5～10%, 10～20%, and over 20%, compared to total length of wire. From the X-ray inspection as shown in Figure 7, MF47F results in 33% of sweeped wire that indicates over 20% of sweeped wire.
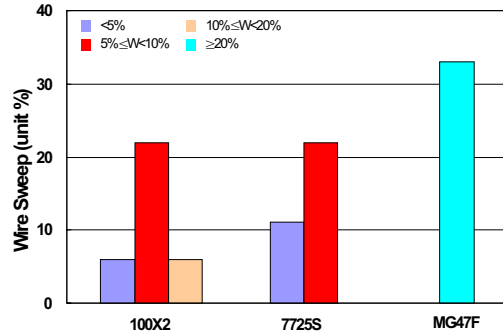

Figure 7 Wire sweep rate (%)

Package Adhesion

In order to analysis how interfacial adhesion strength (Kg_f) between EMC and substrate changes from before and after thermal treatment, package samples are applied to preconditioning steps (85℃/85%RH for 1 hour, and then 3 times reflow at 225℃ peak temperature). Preconditioning drives decrease of interfacial adhesion strength (Kg_f) as shown in Figure 8.
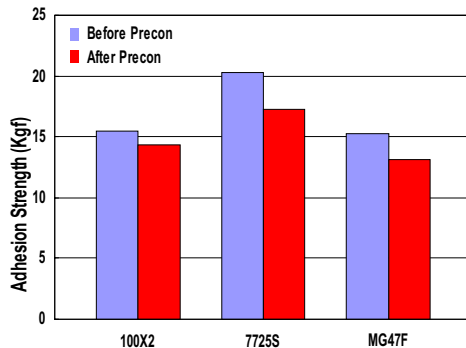
Figure 8 Adhesion strength (Kg_f) before and after preconditioning.

Zyglo Penetration Test

To identify penetration (unit area %) by fluorescent material into package inside, Zyglo as fluorescent material is used to penetration test (100 PSI for 1 hour). Package samples are carried out of mechanical decapsulation after Zyglo penetration test, and measured penetration level of them. Figure 9 shows penetration rate (unit area %) before and after preconditioning. MG47F is archived at about 95% of penetration rate by Zyglo material.
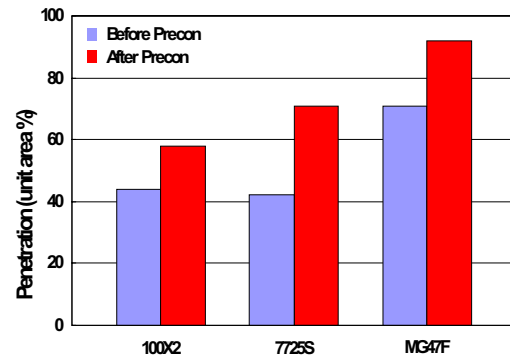

Figure 9 Zyglo penetration rate (unit area %) before and after preconditioning

Table 3 Analysis results for EMCs that have different material properties.

| Response	Condition	100X2	7725S	MG47F
Warpage	Before PMC	1.3208	1.1176	2.2606
(mm)	After PMC	0.8636	0.9906	2.2806
Voiding (unit %)	> 0.508 mm	7.4	11.1	20.4
Wire Sweep (unit %)	<5%	6	11	0
	5%<WS<10%	22	22	0
	10%<WS<20%	6	0	0
	>20%	0	0	33
Adhesion Strength	Before Precon.	15.5	20.3	15.3
(Kgf)	After Precon.	14.3	17.3	13.1
Zyglo Penetration	Before Precon.	44	42	71
(unit area %)	After Precon.	58	71	92

2.3 Process Optimization

In transfer molding process, parameter optimization study to improve package reliability open poses serous obstacles because there exists strong interactions among the parameters. For any given set of parameters, the temperature, velocity, and viscosity of the EMC all changes rapidly as it moves through the runner or gate and into the mold cavity. Based on defined "1L-1D-1A" as geometrical gate design parameter, as well as HC100X2 as the best EMC, design of experiment (D.O.E) is conducted to find optimum molding process window and thereby the relation between process parameters are quantitatively analyzed for package reliability prediction.

Screening D.O.E for main parameter define

To predict a potential influence on package reliability following to molding parameter condition, 2^4 fractional factorial design is performed to identify critical parameters to seriously affecting the molding qualities, such as incomplete fill (unit), voiding (unit), and wire sweep (unit%). As input process variables, clamp force (150～300 KN), transfer pressure (15～45 bar), transfer speed (1～5 mm/s), and mold cavity temperature (155～185 ℃) are considered. This screening DOE consists of 8 experimental runs with 72 sample units per run. From the experiment, it is analyzed that clamp force (KN), transfer speed (mm/s), and mold cavity temperature (℃) are the main process parameters with 90%
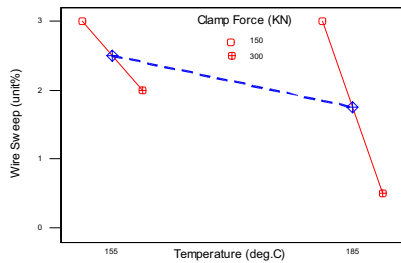
confidence, statistically. Figure 10 gives relative significance of each parameter affecting of relation between input process variables and output quality responses.
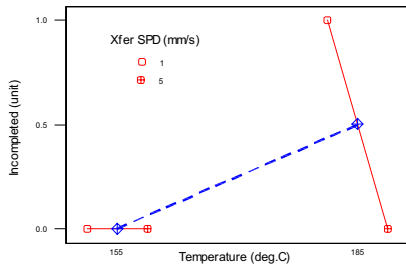
(a) Incomplete fill (unit)
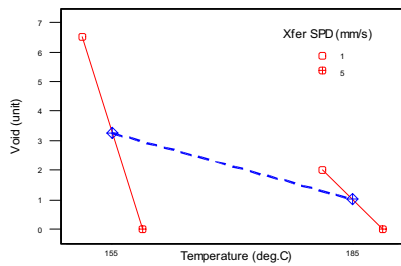
(b) Voiding (unit)
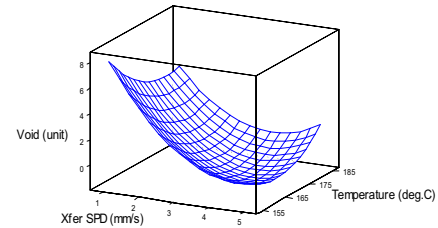

(c) Wire sweep (unit %)

Figure 10 Relation between input process parameters and output quality responses

Optimizing D.O.E for parameter optimization

To find combinations of a number of experimental factors that will lead to optimum responses, Response Surface Methodology (RSM) [7] are used for parameter optimization. The factors defined by screening D.O.E, are utilized for input process variables, such as clamp force (150～300 KN), transfer speed (1～5 mm/s), and mold cavity temperature (155～185 ℃). In order to fit response surfaces, Box-Behnken design [8] listed in Table 4, is selected to analyze quality responses, such as incomplete fill (unit), voiding (unit), and wire sweep (unit%). RSM consists of 15 experimental runs with 72 sample units per run.

Table 4 A three-variable Box-Behnken design

| | Input Variables | | |
	Clamp (KN)	Xfer SPD (mm/s)	Temp (deg.C)
1	-	0	-
2	-	-	0
3	+	+	0
4	0	+	+
5	0	0	0
6	+	0	+
7	0	0	0
8	0	-	-
9	-	0	+
10	0	+	-
11	0	0	0
12	+	0	-
13	0	-	+
14	+	-	0
15	-	+	0

Estimated Regression Coefficients for Void

Term	Coef	StDev	T	P
Constant	-0.385	0.8615	-0.446	0.666
Xfer SPD	-2.75	0.634	-4.337	0.002
Temp	-0.5	0.634	-0.789	0.451
Xfer SPD*Xfer SPD	2.423	0.9305	2.604	0.029
Temp*Temp	1.423	0.9305	1.529	0.161
Xfer SPD*Temp	1.25	0.8966	1.394	0.197

S = 1.793   R-Sq = 76.9%   R-Sq(adj) = 64.1%

Analysis of Variance for Void

Source	DF	Seq SS	Adj SS	Adj MS	F	P
Regression	5	96.391	96.391	19.278	5.99	0.01
Linear	2	62.5	62.5	31.25	9.72	0.006
Square	2	27.641	27.641	13.821	4.3	0.049
Interaction	1	6.25	6.25	6.25	1.94	0.197
Residual Error	9	28.942	28.942	3.216		
Lack-of-Fit	3	13.942	13.942	4.647	1.86	0.237
Pure Error	6	15	15	2.5		
Total	14	125.333				

Figure 11 Response surface analysis for package voiding

In case of incomplete fill (unit), it does not observed from all of experimental runs. For the package voiding (unit), Figure 11 illustrates fitted regression model with estimated regression coefficients for voiding (unit). As depicted in Figure 11, 0.237 of lack-of-fit does not significant, statistically at the 95% confidence. In addition, R^2 (=76.9 %) denotes that regression model explains package voiding phenomenon at about 77%.

Figure 12 demonstrates fitted regression model with estimated regression coefficients for wire sweep (unit%). As presented in Figure 12, 0.751 of lack-of-fit does not

significant, statistically at the 95% confidence. R^2 (=75.5 %) elucidates regression model is acceptable to explain wire sweep phenomenon at about 76%.
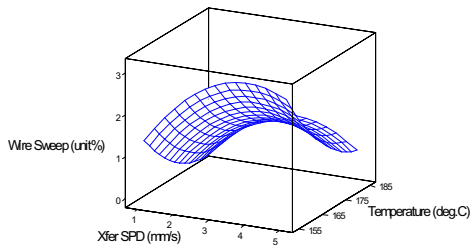
Estimated Regression Coefficients for W/S

Term	Coef	StDev	T	P
Constant	1.6154	0.3129	5.163	0.001
Xfer SPD	0.5	0.2303	2.171	0.058
Temp	-0.875	0.2303	-3.8	0.004
Xfer SPD*Xfer SPD	-0.8269	0.3379	-2.447	0.037
Temp*Temp	0.4231	0.3379	1.252	0.242
Xfer SPD*Temp	-0.25	0.3256	-0.768	0.462

S = 0.6513   R-Sq = 75.5%   R-Sq(adj) = 61.9%

Analysis of Variance for W/S

Source	DF	Seq SS	Adj SS	Adj MS	F	P
Regression	5	11.7827	11.7827	2.3565	5.56	0.013
Linear	2	8.125	8.125	4.0625	9.58	0.006
Square	2	3.4077	3.4077	1.7038	4.02	0.057
Interaction	1	0.25	0.25	0.25	0.59	0.462
Residual Error	9	3.8173	3.8173	0.4241		
Lack-of-Fit	3	0.6506	0.6506	0.2169	0.41	0.751
Pure Error	6	3.1667	3.1667	0.5278		
Total	14	15.6				

Figure 12 Response surface analysis for wire sweep

Using statistical regression models from experiment for both voiding (unit) and wire sweep (unit%), it is possible to obtain a collection of contour lines for mapping the response surface to determine appropriate optimum response. Optimum responses that are depicted A and B in Figure 12, are illustrates that voiding and wire sweep can be a minimum.
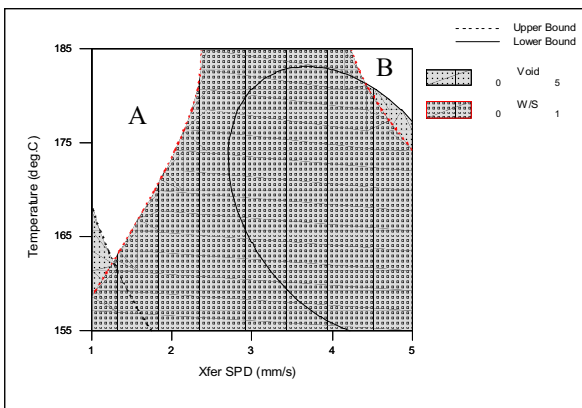

Figure 13 Contour plot by fitted regression model

Even though response surface (A) indicates one of optimum parameter windows, it requires at least $10 \sim 22.5$ seconds of EMC filling time, and causes increase of overall process cycle time. Accordingly, response surface (B) is selected to optimum parameter window area as is shown in contour plot in Figure 13.

From 30 Lots (1 Lot = 2880 units) sample inspection from optimum process window B (185 ℃ of mold cavity temperature, 5 mm/s of transfer speed), it is validated that voiding defect is reduced from 25000 ppm to 300 ppm, as well as wire sweep is minimized from 200 ppm to 20 ppm.

Conclusion

As geometrical gate design parameters, "1L-1D-1A" scale reduces flow-induced package stress, such as interfacial delamination between EMC and substrate, otherwise increases EMC concentration level that has minimum opportunity of internal voiding of package. From the analysis of EMC influences on package reliability, HC100X2 is defined as the most suitable EMC compared to other candidates. In addition, screening D.O.E identifies mold cavity temperature (℃), transfer speed (mm/s), and clamp force (KN) as main process parameters. Based on the key contributors as defined by screening D.O.E, 185 (℃) of mold cavity temperature, 5 (mm/s) of transfer speed are determined as the optimum parameters window from RSM in the transfer molding process.

References

[1] Y.Feng, V.R.Raju and E.Suhir, "Moisture Induced Failures of Plastic Packages of IC Devices", ASME International Mechanical Engineering Congress and Exposition, pp89-140, 1997

[2] L.S. Turng and V.W. Wang, "On the simulation of Microelectronic Encapsulation with Epoxy Molding Compound", ANTEC, pp84-88,1992

[3] In Seongoo Lee, "Computer Simulation of Transfer Molding in IC Packaging, Packaging Technology, SEMICON96, pp141-147,1996

[4] A. Brent Strong, *Plastics Materials and Processing*, pp466-473, 1996

[5] Wei H. Koh, Beverly H. Tai, Elizabeth A. Kolawa, "Low Stress Encapsulants for Reduced Failures in Plastic Packages", International Mechanical Engineering Congress and Exposition, pp1-5, 1995

[6] Louis T. Manzione, *Plastic Packaging of Microelectronic Devices*, pp256-260,1990

[7] George E.P.Box, William G.Hunter, J.Stuart Hunter, *Statistics for Experimenters An Introduction to Design Data Analysis, and Model Building*, pp374-539,1978

[8] Douglas C. Montgomery, *Design and Analysis of Experiments*, pp575-611,1997

Electrical Characteristics of Single and Coupled Stripline
on Meshed Ground Plane in High-Speed Package

Heeseok Lee* and Joungho Kim**

Terahertz Media and System Laboratory, Division of Electrical Engineering,
Department of Electrical Engineering and Computer Science, Korea Advanced Institute of Science and Technology,
373-1 Kusong, Yusong, Taejon 305-701, Korea, Tel) +82-42-869-5458, Fax) +82-42-869-8058
E-mail) heeslee@eeinfo.kaist.ac.kr* , j\oungho@ee.kaist.ac.kr **

Abstract

In high-speed package, the high-frequency characteristic of the interconnection structure becomes more and more important. In this paper, the propagation characteristics of the stripline placed on the meshed ground plane (SMEP) will be determined. The effective dielectric constant and the characteristic impedance of the single SMEP are determined by utilizing the full-wave analysis. For the longitudinally periodic structure modeling of SMEP, the finite-difference time-domain method based on the Floquet's theorem is used. The slow wave effect and the high impedance characteristic are observed. In addition to the single SMEP analysis, the propagation and coupling property of the coupled SMEP is also presented, which is very important in the cross-talk modeling.

Introduction

The last several years have seen significant improvements in microprocessor performance, and the expectation is that these performance trends will be maintained. Core speeds have exceeded the 1 GHz mark. Front-side bus speeds will soon go beyond 400 MHz; and many specialized buses operate at much higher data transfer rates. At the same time, the environment in which this type of performance must be enabled has become increasingly challenging. Voltage levels have continued to decrease with each silicon technology generation to the point that <1 V technologies are not too far out in the future. With tremendous increases in on-die transistor density, power levels have escalated exponentially to the point that they will soon surpass 100 W for many high-end microprocessors. This environment presents challenges for all aspects of electrical design of package-level interconnection structures. Lower voltage levels and faster bus speeds mean that noise and timing budgets are tighter. Higher power levels create challenges in power delivery through the package interconnect to the microprocessor core. Faster clock speeds and higher power levels create signal integrity (SI) and crosstalk challenges. In today's challenging high-speed microprocessor environment, a careful electrical design for the package-level interconnection structure can enable superior system performance while a poor design can limit system performance. Increased microprocessor core and bus speeds, decreased voltages, and increased power levels all present unique challenges to the package designer trying to ensure that electrical performance criteria are met. All of these areas require that the designer be very aware of the electrical characteristics and requirements of the rest of the system.

Although package designer and board designer have used microstrip line and stripline, the new transmission line structures are needed for the special requirement of the high-speed circuit and system. For the special purpose in the high-speed package and board, a couple of modified stripline structures with periodically varying boundary condition have been introduced. Among these, stripline on meshed ground plane (SMEP) will be discussed in this issue. Although an optimum performance of stripline is provided by using a solid ground plane, its employment might not be implemented due to the interlayer interconnection requirement or mechanical integrity problem.[1-11] In order to overcome these drawbacks, a particular grounding structure used in the multiplayer-board application is formed by perforated ground plane. In this environment, the characteristic impedance of the stripline is changed, which must be carefully studied in the aspect of signal integrity.

Stripline on Meshed Ground Plane (SMEP)

The effect of periodically perforated ground planes on the transmission characteristic of a stripline must be carefully determined. Interconnects in an electronic packages are usually modeled as either microstrip line or stripline transmission line. Ideally, these transmission line configurations have solid ground planes, but in real situation the ground planes often have perforations. These meshed structures are required to satisfy the mechanical reliability and the interlayer interconnections. The meshed ground planes are found primarily in the multi-layered low temperature co-fired ceramic (LTCC) substrtrate. Hence, it is very important to find out how the electrical properties of a stripline changes as a function of the geometry of mesh on the ground planes.

While the traditional transmission line structure has uniform two-dimensional cross-section, the SMEP is three-

dimensional structure. Although uniform transmission line can be analyzed in two-dimensional domain, this kind of the periodically varying structure requires three-dimensional full-wave field solving to include the effect of the longitudinal discontinuities. Usually, the propagating modes can be considered to be the Floquet's mode with the assumption of the infinitely repeated periodic structure, as assumed in transmission line theory.[12] In this issue, the electrical characteristics of the SMEP will be determined by utilizing the finite-difference time-domain (FDTD) method based on the Floquet's theorem, which gives the intrinsic propagation property of the SMEP as a transmission line and reduces computational domain[13-16].

The effect of meshed ground plane structure on the phase velocity of the SMEP will be obtained. When the signal line placed on the perforation of the meshed ground plane, the slow wave effect is increased. Besides the high-impedance and slow-wave property of single SMEP, the cross-talk characteristic of the coupled SMEP will be also considered. This study must help latest high-speed package design including multilayered LTCC substrate technology.
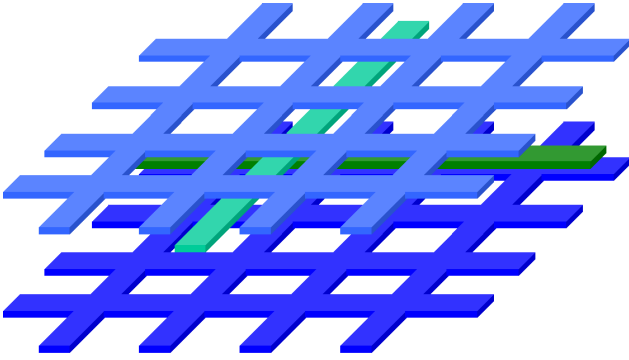
Figure 1. Stripline on meshed ground plane (SMEP)

Modeling Methodology based on the Floquet's Mode Analysis using FDTD method

For electromagnetic modeling, the repeated boundary condition of the stripline with meshed ground plane (SMEP) attracts the application of the Floquet's theorem.[13] In this paper, the time-domain method, FDTD, is utilized to get the full wave solution of the periodically varying stripline structures, SMEP. Since, as well known, the stripline discontinuity structure requires three-dimensional full wave electromagnetic field solving, FDTD simulation based on the Floquet's theorem [15,16] is utilized for wave propagation characteristics of the SMEP structure.

$$\begin{Bmatrix} \vec{E}(x,y,z,t) \\ \vec{H}(x,y,z,t) \end{Bmatrix} = \begin{Bmatrix} \vec{E}_p(x,y,z,t) \\ \vec{H}_p(x,y,z,t) \end{Bmatrix} e^{j\beta z} \quad (1)$$
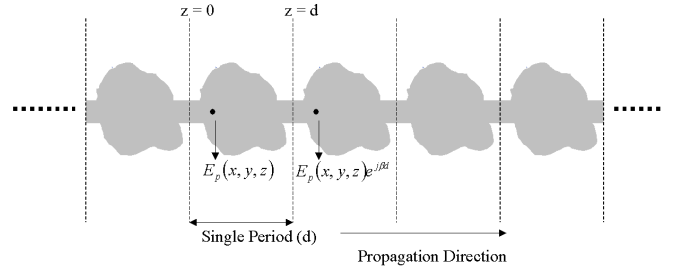

Figure 2. Arbitrary interconnecting structure with longitudinally periodic boundary condition. The wave propagation characteristic in this kind of structure can be determined based on the Floquet's mode analysis. The longitudinal direction is parallel to Z-axis. The wave function for the guided wave in a longitudinally periodic waveguide can be represented by the periodic function multiplied by the phase function exp(jβz).
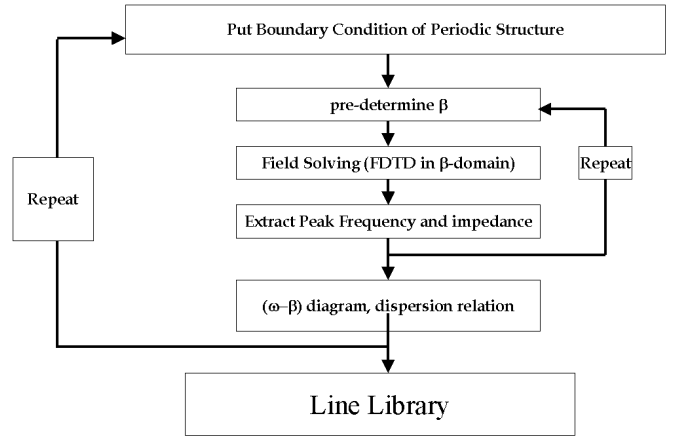

Figure 3. Routine for Floquet's mode dispersion analysis using FDTD method

For the FDTD computation in transformed β -domain with the periodic function, the longitudinal spatial-derivative operator $\partial/\partial z$ must be replaced by $\partial/\partial z + j\beta$. While the FDTD method originally computes time-domain real function, the time-domain complex function must be computed to restrict its computational domain to single period of an LPW by the longitudinal periodicity in the β -domain. The presented FDTD method calculates the electric field $\vec{E}(x,y,z,t)$ and the magnetic field $\vec{H}(x,y,z,t)$ represented by the same way as (1) just in a single period ($z \in [0,d]$) with a predetermined propagation constant β and periodic boundary condition demonstrated in Fig.2. The update equations are given in (2) for the real part of H_x component.

$$H^r_{x(p,q+0.5,r+0.5,n+0.5)}$$

$$= \left| \frac{\Delta t}{\mu} \times \left[\begin{array}{c} H^r_{x(p,q+0.5,r+0.5,n-0.5)} - \\ \left(\dfrac{\beta}{2} \left(E^i_{z(p,q,r+0.5,n)} + E^i_{z(p,q+1,r+0.5,n)} \right) \right) \\ + \dfrac{E^r_{z(p,q+1,r+0.5,n)} - E^r_{z(p,q,r+0.5,n)}}{\Delta y} \\ - \dfrac{E^r_{y(p,q+0.5,r+1,n)} - E^r_{y(p,q+0.5,r,n)}}{\Delta z} \end{array} \right] \right| \qquad (2)$$

In (2), Δt is the time step and Δy and Δz are the spatial mesh sizes along y-axis and z-axis, respectively. The $H^r_{x(p,q,r,n)}$ represents the real part of $H_x(p\Delta x, q\Delta y, r\Delta z, n\Delta t)$, where p, q, r and n are integers for index. The finite-difference equations for the remained components can be derived in the same manner. With a β, the FDTD simulation is performed to get the impulse response. Although the initial field distribution can be obtained by static field solver for the reduction of the transient time, the initial electric field distribution at t = 0 was assumed to be uniform along the SMEP to validate the computational robustness of the FDTD method. The peak frequencies of the modes corresponding to the predetermined propagation constant β used in each FDTD run is obtained by the fast Fourier transform (FFT) of the calculated impulse response, as presented in [15]. The FDTD simulation and the followed FFT for each β give the dispersion diagram, which is presented in Fig. 3.

Single SMEP analysis

In this section, the effect of the meshed ground plane on the signal transmission property of the stripline will be discussed based on the Floquet's mode analysis using FDTD method. First, the dispersion analysis was performed with the SMEP, in which the width of the signal line, W, is selected between 0.25 mm and 0.50 mm. and the height of the FR-4 substrate is 1.0 mm. In the FDTD simulation, the dielectric constant of the FR-4 is assumed to be 4.5. The geometry of the perforation on the meshed ground plane is presented in the Fig. 4. To observe the effect of the position of the signal line with respect to the perforated pattern of the meshed ground plane, the propagation characteristics for two cases shown in Fig. 4 is determined. With the presented conditions, the effective dielectric constant given by (3) and the characteristic impedance for presented SMEPs is calculated based on the Floquet's mode analysis using time-domain method. In (3), c_0 is the phase velocity in free-space, 3×10^8 m/s.

$$\varepsilon_{effective} = \left(\frac{\beta c_0}{\omega} \right) \qquad (3)$$
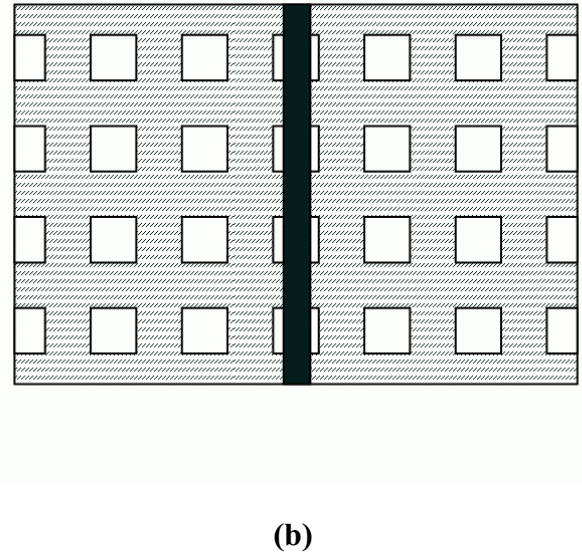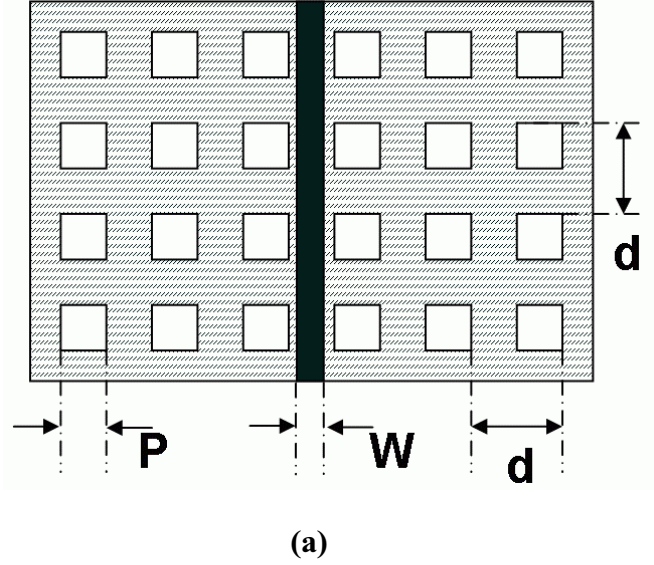

(a)

(b)

Figure 4. Schematic of SMEP. While (a) indicates the SMEP located on solid region of the meshed ground plane, (b) shows the SMEP placed on perforated region of the meshed ground plane. The SMEP is implemented with the 1mm-thick FR-4 substrate. The intrinsic dielectric constant of the used FR-4 substrate is 4.5. The signal line is placed in the middle of the top and bottom ground plane, which means that the height of the signal line with respect to the bottom ground plane is 0.5mm. The top and bottom ground plane are identical. In this study, the period of the meshed ground plane, d, is fixed to be 0.75mm.

The larger mesh size (P) of the perforated ground gives the slower and higher impedance SMEP, as shown in Fig.5-8. Figure 5 and 7 show the effective dielectric constant of the SMEP with different values of the signal width (W) and the perforation (P). The wave propagating through the SMEP is retarded by the disturbance of the perforated ground plane. The current on the meshed ground plane flowing round the perforation results in the slow wave. The roundabout current path makes the inductance of the ground plane larger, which results in high impedance property of SMEP, as shown in Fig. 6 and 8. As can be observed in Fig.6 and 8, the relation of the perforation and the impedance is not linear. When the perforation ratio (P/d) is over 0.5, the characteristic impedance rapidly increases. The SMEP placed on the perforated region of the meshed ground plane shown at Fig.4(b) has higher impedance and larger effective dielectric constant than the SMEP located on the solid region given at Fig.4(a), as shown in Fig.9 and Fig. 10, respectively. When the signal line placed on the perfored region of the meshed ground plane, the slow wave effect is increased and the inductance generated by the imperfect ground plane becomes larger. In other words, the phase velocity of the SMEP is the function of the position of the signal line with respect to the perforation of the meshed ground plane.

Figure 6. Characteristic impedance (Z$_0$) of the SMEP shown at Fig.4(a) for seven different line widths. They are obtained at 4.5 GHz by FDTD simulation when the signal trace is placed on the perforated region of the meshed ground plane.
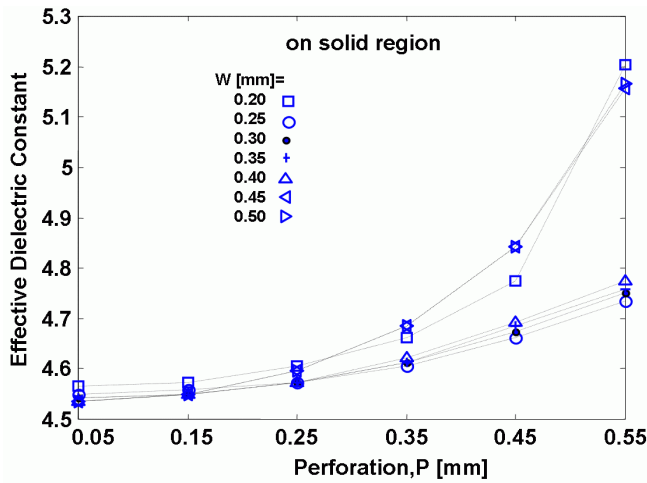
Figure 5. Effective dielectric constant with respect to the size of the perforation on the ground plane. They are obtained at 4.5 GHz by FDTD simulation when the signal trace is placed on the perforated region of the meshed ground plane. (SMEP shown at Fig.4(a)).
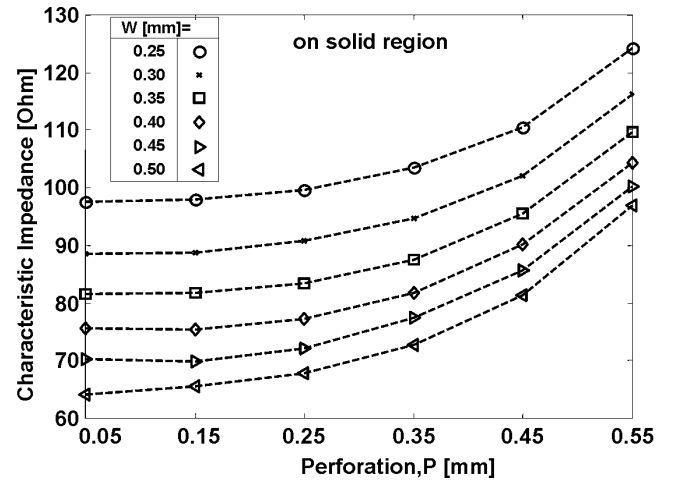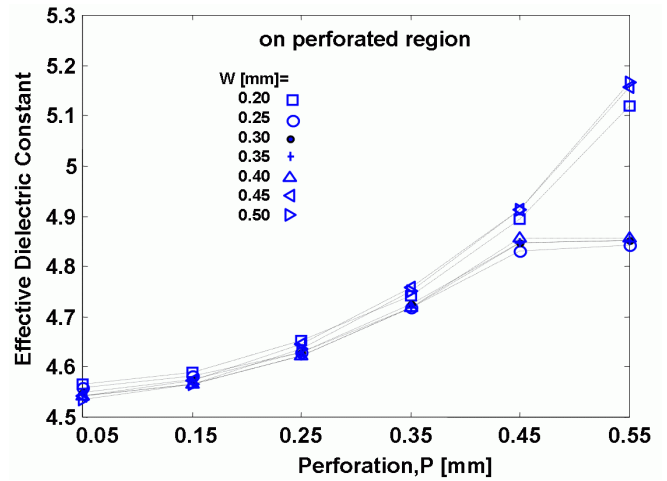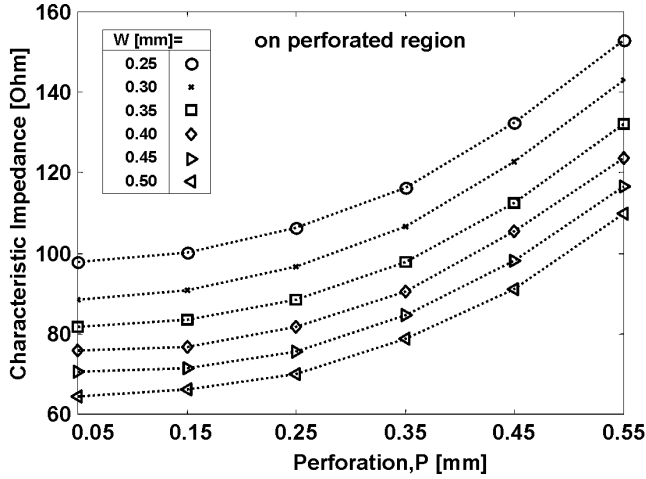

Figure 7. Effective dielectric constant with respect to the size of perforation (P) on the ground plane. They are obtained at 4.5 GHz by FDTD simulation when the signal trace is placed on the perforated region of the meshed ground plane. (SMEP shown at Fig.4 (b))

Figure 8. Characteristic impedance (Z_0) of the SMEP shown at Fig.4(a) for seven different line widths. They are obtained at 4.5 GHz by FDTD simulation when the signal trace is placed on the perforated region of the meshed ground plane.
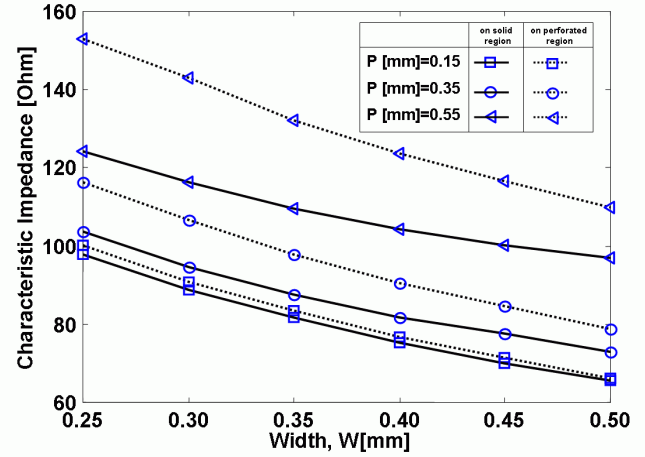
Figure 10. Calculated characteristic impedance (Z_0) at 4.5 GHz with respect to the width of the signal line, W. As shown, the characteristic impedance of the SMEP placed on perforated region is higher than that of the SMEP placed on solid region.
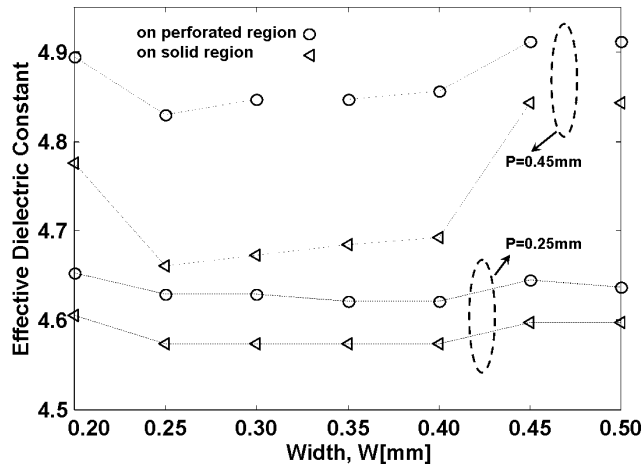

Figure 9. Effective dielectric constant with respect to the width of the signal line, W. They are obtained at 4.5 GHz by FDTD simulation. As shown, the SMEP placed on perforated region is slower than the SMEP placed on solid region.

Coupled SMEP analysis

Classically, the propagating mode along the coupled transmission line has been analyzed using even mode and odd mode decomposition. Rigorously, the coupled SMEP is not always symmetric, which makes the even/odd mode decomposition difficult. However, the propagation property of the coupled SMEP will be analyzed utilizing simple even/odd mode analysis, in this study. In the following analysis of the coupled SMEP, the even/odd modes are taken under the assumption that the ground plane is solid. Although the orientation of the coupled SMEP with respect to the perforation of the meshed ground plane should be considered as presented at the single SMEP analysis, the effect of the position of the signal lines on the propagation property will be ignored in this time.

Figure 11 shows the geometry of the coupled SMEP analyzed in this study. The substrate structure is identical to the case given in the single SMEP analysis. As shown at Fig. 12, the slow wave effect is observed. While the stripline on the solid ground plane filled by homogeneous material has one phase velocity for even mode and odd mode, the coupled SMEP has two different effective dielectric constants for even mode and odd mode, as shown at Fig. 12. The phase velocity mismatch in the coupled SPEP is caused by the perforated ground plane. The SMEP is no longer able to be treated electrically as a transmission line structure filled with homogeneous material. The slower even mode observed at Fig.12 can be explained based on the coupled line theory of microstrip line. In the coupled microstrip line structure, since the more field is confined in the dielectric substrate for even

mode rather than odd mode, its even mode is slower than its odd mode. In other words, since the electric field distribution of odd mode is concentrated at the interface of the dielectric substrate and the air, its effective dielectric constant is smaller. For the coupled SMEP, the even mode is slower than the odd mode. Since the field distribution guided by odd mode is confined between two signal traces, the perforation in the ground plane gives relatively small effect on the odd mode propagation. As shown in Fig. 12, the larger perforation (P) increases the difference of the effective dielectric constant for two propagating modes, which assures the effect of the perforation on the phase velocity mismatch between even mode and odd mode.
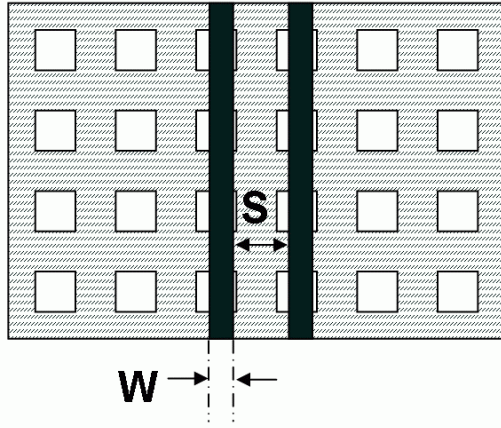
Figure 11. Schematic of the coupled SMEP. W is the width of the signal line. S indicates the separation of two signal lines.
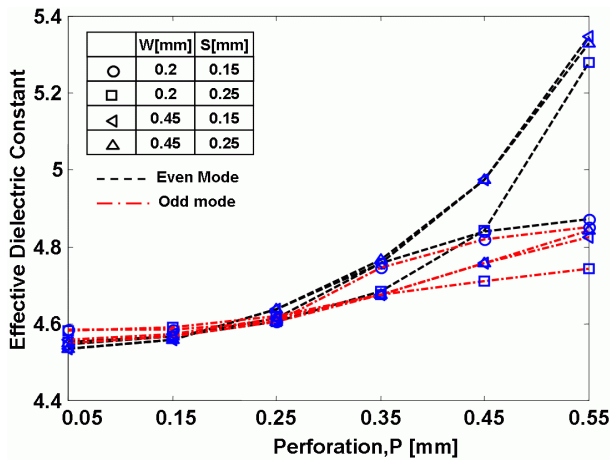
Figure 12. Calculated effective dielectric constant of four coupled SMEPs at 4.5 GHz with respect to the size of the perforation on the ground plane. As observed, the even mode is slower than the odd mode.
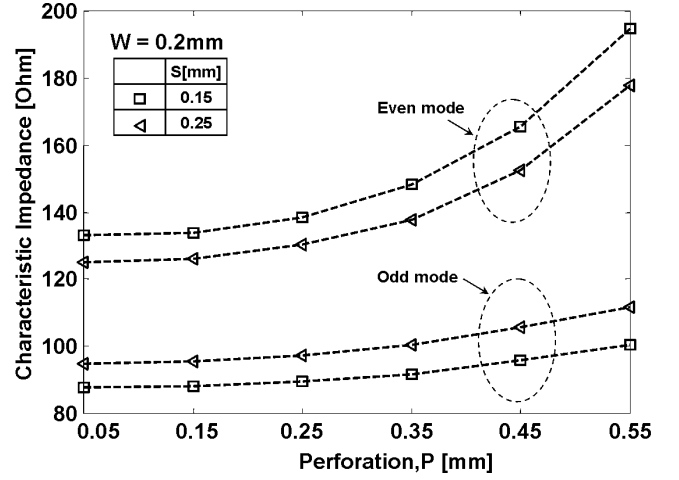

Figure 13. Calculated characteristic impedance for SMEP with W = 0.2 mm at 4.5GHz. The even mode impedance (Z_{even}) is higher than the odd mode impedance (Z_{odd}).
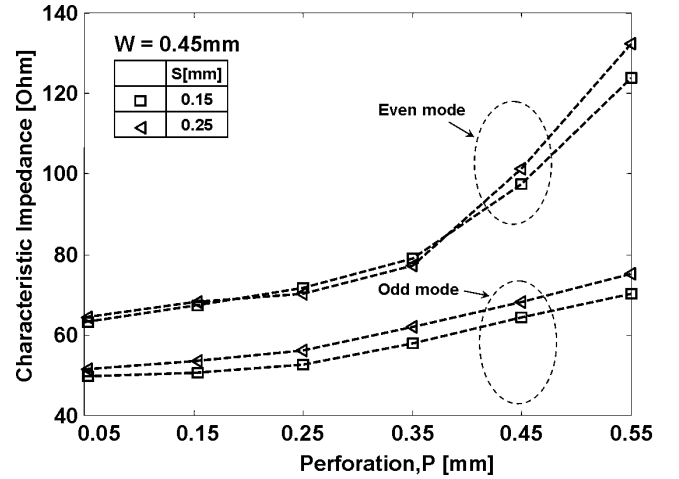

Figure 14. Calculated characteristic impedance for SMEP with W = 0.45 mm at 4.5GHz. The even mode impedance (Z_{even}) is higher than the odd mode impedance (Z_{odd}).

The characteristic impedance is presented in Fig.13 and 14. The even-mode impedance (Z_{even}) is higher than the odd mode impedance (Z_{odd}). As determined in terms of the effective dielectric constant, the higher Z_{even} is caused by the effect of the perforation on the ground plane. The even mode impedance is more sensitive to the increase of the perforation (P), as shown in Fig.13 and 14. Figure 15 shows the coupling coefficient defined by (4). The small value of separation between the signal lines indicated by S gives the large value of the coupling coefficient, as expected.

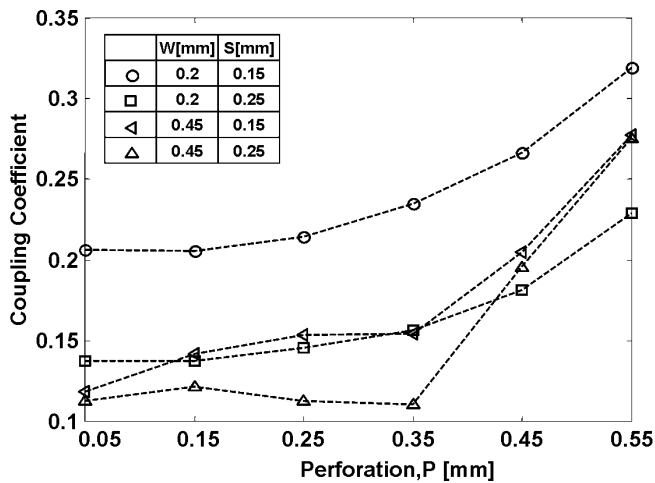$$K_C = \frac{Z_{even} - Z_{odd}}{Z_{even} + Z_{odd}} \tag{4}$$

Figure 15. Calculated coupling coefficient (K_C) of four coupled SMEPs at 4.5GHz. As observed, the coupling coefficient of the SMEPs with P =0.55 mm is maximum.

Conclusions

In conclusion, the propagation characteristic of the single and the coupled SMEP was determined based on the Floquet's mode analysis using FDTD method. The wave propagation through the SMEP becomes slow, which results in large effective dielectric constant. The characteristic impedance of the SMEP becomes higher than that of the stripline placed on the solid ground plane. Together with the single SMEP, the crosstalk modeling is performed with the coupled SMEP analysis. In the high-speed package design, the variation of the characteristic impedance and the phase velocity of the SMEP must be carefully considered in the aspect of signal integrity and crosstalk.

References

1. Rao R. Tummala, Fundamentals of microsystems packaging, McGraw-Hill (New York 2001), pp. 322-326
2. M. Gribbons, A. Cangellaris, and J. Prince, "Finite-difference time-domain analysis of pulse propagation in multichip module interconnects," IEEE Trans. Components, Hybrids, and Manufacturing Technology, Vol. 16, no.5, pp.490-498, Aug. 1993.
3. C.P.Chien, A.F.Burnett, J.M.Cech, andM.H.Tanielian, "The signal transmission characterizations of embessed microstrip transmission line over a meshed ground plane in copper/polyimide multichip module," IEEE Trans. CPMT-B, Vol.17, No.4, Nov.1994, pp.578-583.
4. A.W.Mathis and A.F.Peterson, "Modeling and analysis of interconnects within a package incorporating vias ans a perforated ground plane," IEEE Electronic Components and Technology Conference 1996 Proceeding, pp.984-990.
5. P. Bernardi, R. Cicchetti, and Antonio Faraone, "A full-wave characterization of an interconnecting line printed on a dielectric slab backed by a gridded ground plane," IEEE Trans. Electromagnetic Compatibility, vol.38, no.3, pp.237-243, Aug. 1996
6. W.Y.Tam and Y.Chen, "Analysis of microstrip lines on a perforated ground using reciprocity method," 1997 Asis Pacific Microwave Conference Proceeding, pp.425-428.
7. Guangwen Pan, X. Zhu, and B. K. Gilbert, "Analysis of transmission lines of finite thickness above a periodically perforated ground plane at oblique orientations," IEEE Trans. Microwave Theory and Tech., vol.43, no.2, pp.383-393, Feb. 1995
8. M. Kahrizi, T. K. Sarkar, and Z. A. Markevic, "Dynamic analysis of a microstrip line over a perforated ground plane," IEEE Trans. Microwave Theory and Tech., vol.42, no.5, pp.820-825, May. 1994.
9. Sifen Luo, Jyh-Ming Jong, and V.K.Tripathi, , "Crosstalk in coupled interconnects with meshed ground planes," IEEE Multi-Chip Module Conference (MCMC), 1994. Proceedings, pp.132 –137.
10. Y.S.Tsuei, and A.C.Cangellaris, "Quantification of interconnect coupling mechanisms in multilayer substrates with perforated ground planes," IEEE Electronic Components and technology Conference 1997 Proceeding, pp.810-816.
11. Jae-Kyung Wee, Young-Hee Kim, Yong-Ju Kim, Pil-Soo Lee, Yong-Je Jeon, Jo-Han Kim, Han-Sub Yoon, and Jin-Yong Chung, "A study of underlayer geometry effects on interconnect lines characteristics through S-parameter measurements," IEEE Electronic Components and Technology Conference 2001, pp.1290-1294.
12. R. E. Collin, Foundation of microwave engineering, 2nd Ed., McGrawHill, 1992. Chapter 7.
13. A. C. Cangellaris, M. Gribbons, and G. Sohos, "A hybrid spectral/FDTD method for the electromagnetic analysis of guided waves in periodic structures," IEEE Microwaves and Guided Wave Letters, vol.3, no.10, Oct. 1993. pp.375-377.
14. M. Celuch-Marcysiak and W. K. Gwarek, "Spatially looped Algorithms for time-domain analysis of periodic structures," IEEE Trans. on Microwave Theory and Techniques, Vol.39, April, 1995. pp.860-865.
15. Heeseok Lee and Joungho Kim, "Modified Yee's cell for finite-difference time-domain modeling of periodic boundary guiding structure," 2001 IEEE MTT-S International Microwave Symposium, May 2001, pp. 889-892.
16. Heeseok Lee, Namhoon Kim, and Joungho Kim, "Unit-cell modeling of meander delay line based on finite-difference time-domain method and Floquet's Theorem," to be presented at IEEE 10th Topical Meeting on Electrical Performance of Electronic Packaging (EPEP 2001), Cambridge, MA., Oct. 2001.

Adaptation of neural network and application of digital ultrasonic image processing for the pattern recognition of defects in Semiconductor

Jae-Yeol Kim, Hyun-Jo Jeong, Hun-Cho Kim, Chang-Hyun Kim

Chosun University, The Division of Mechanical Engineering
375, Seosuk-dong, Kwangju 501-759, Republic of Korea
email : jykim@chosun.ac.kr , phone & fax : 82-62-230-7035
Wonkwang University, The Division of Mechanical Engineering
The Korea Chamber of Commerce & Industry, Kwangju
Chosun Graduate School, The depature of Precision Mechanical Engineering

Abstract

In this study, the classification of the artificial defects in semiconductor devices are performed by using the pattern recognition technology. For this target, the pattern recognition algorithm including the user made software was developed and total procedure including Image Procesing and Self-organizing map was treated by Backpropagation neural network. Where, Image Processing was made up ultrasonic image acquisition, equalization filtering, binary processing and edge detection. Especially, Image Processing and Self-organizing map were compared as preprocessing methods for the reduction of dimensionality as input data into multi-layer perceptron or Backpropagation neural network. Also, the pattern recogniton technique has applied to classify two kinds of semiconductor defects : crack and delamination. According to these results, it was found Self-organizing map, it provided the recognition rates of 83.4% and 75.7% for delamination and crack, repeatedly while BP provided 100% recognition rates for the results.

1. Introduction

Semiconductor components are essential to electronic devices such as medical equipments, military weapons and so on. Therefore, defects in semiconductor components may affect the mechanical or electronic performance of devices. For these reason, it is very important to detect such defects in the manufacturing process. Some detection methods for semiconductor components largely depend on nondestructive tests and have been accomplished by human experrience. Recently, defects detection system for semiconductor like SAT(Scanning Acoustic Tomograph) has been adopted in the actual manufacturing process. Manufacturers like HITACHI and SONIX provide powerful image results with users of ultrasonic nondestructive methods. It help users to analyze displayed results on the screen.

The purpose of this research is to develop an intelligent expert system for the detection and evaluation of defects in semiconductor package by using digital image processing off ultrasonic signal and neural networks. By doing this, the manufacturing process can be standardized in order to appraise the patterns of defects, based on various information. To accomplish this purpose, image processing and neural network is applied to the SAT image and an intelligent expert system for semiconductor defects classification is developed, which can feedback standardized information on defects to manufacturing process. If an appropriate evaluation system during mass production is established for the detection and evaluation of semiconductor defects, precise goods with high quality will be rapidly produced. Also, such an evaluation system can be helpful to set up the proper work processing to remove basic defects from the actual manufacturing process.

2. Image Preprocessing

In this research, image preprocessing is the procedure including the method of dimensionality reduction for input into neural network. And we applied two methods in this research. One is the application of digital ultrasonic image processing and the other is the adaptation of self-organizing map, where, Self-organizing map is one of neural networks.

2.1 Image Acquisition

When we talk about digital image, each point is called pixel on image plane. And light density is saved into memory or backing memory as digit with some section.
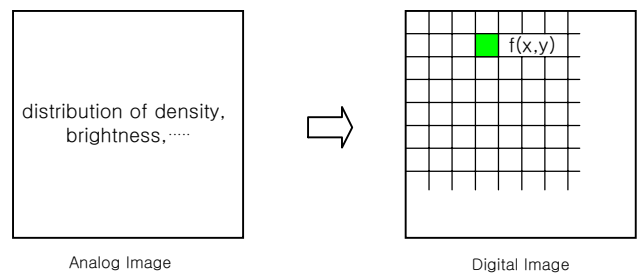

Fig.1 Coordinates on image plane

Light intensity is meant brightness of each pixel that is marked as function of $f(x, y)$ in fig.1. And light density is transformed into value, these process is called digitization. Acquired images are taken with gray level was expressed as value between 0 and 256.

2.2 Image Filtering

The process acquiring image from object is composed of sampling, quantization, communication, and so on. Through this process, noise image is included to original image. Therefore, we have to remove this noise image in original image, applied neighborhood averaging method for removing noise image from acquired image, that is, original image.

In $f(x, y)$ of image with size N×N, neighbor part with pixel of n×m is averaged, and this part is alternated with gray level of pixel (x, y) for each pixel element (x, y). This process

is neighborhood averaging method. If this equalizing image is $g(x, y)$, we can express as follow equation.

$$g(x, y) = \frac{1}{M} \sum_{(n, m) \in s} f(n, m) \qquad (1)$$

Where, M is number of cell with size n×m in some part, S is expressed a set of pixel in some part.

2.3 Binary Processing

Binary process is a conversion from gray image (or RGB image) to binary image, is a typical method separating object in image from the scene of image. Where, threshold is related with t in function of $f(x, y)$, we can express as follow equation.

$$f_t(x, y) = 1 \quad f(x, y) \geq t$$
$$f_t(x, y) = 0 \quad f(x, y) \leq t \qquad (2)$$

Where, $f_t(x, y)$ is a binary image that is determined by threshold t of $f(x, y)$, $f(x, y)$ is a gray image of (x, y). After this process, $f_t(x, y)$ is transformed to binary image with 0 or 1.
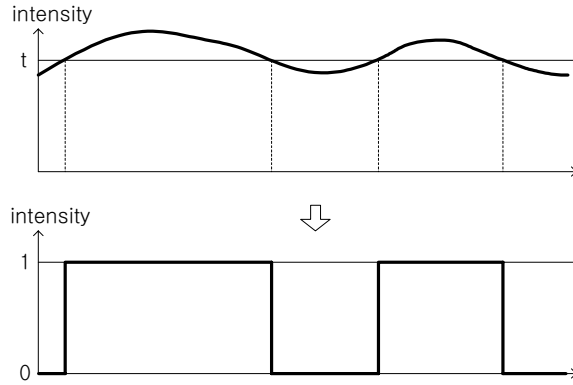
Fig.2 Binary conversion from gray image

2.4 Edge Detection

Edge line is the feature including the boundary of each pixel, is expressed the uncontinous line about brightness of pixel.
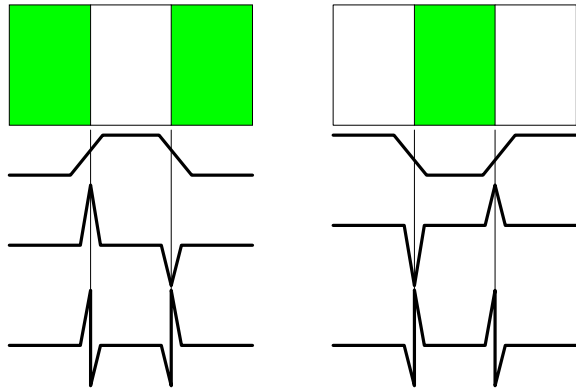
Fig.3 Binary conversion from gray image

In this research, information of image is the input vector for backpropagation neural network. The method of Edge detection is applied as 4 – connected neighborhoods. The case

of coordinates with $(x, y), (s, t)$, Euclidean distance between p and q is expressed as follow equation.

$$D_e(p, q) = [(x - s)^2 + (y - t)^2]^{\frac{1}{2}} \qquad (3)$$

Distamce D_4 between p and q is defined as followed.

$$D_4(p, q) = |x - s| + |y - t| \qquad (4)$$

Distance D_4 is equal to radious r from center (x, y), or is small to radious r from center (x, y). These pixels are formated as the shape of diamond.

2	1	2
1	0	1
2	1	2

Fig.4 Binary conversion from gray image

2.5 Self-Organizing Map

In this research, self-organizing map is the input vector for backpropagation neural network. This self-organizing map is applied as the process of dimensionality reduction for image.
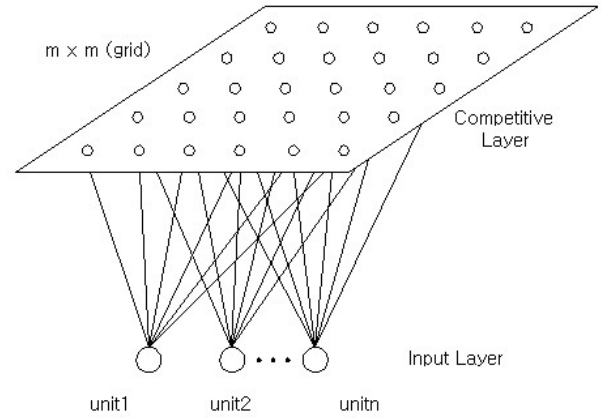

Fig.5 Kohonen neural network

Self-Organizing Map by Kohonen is neural network with two-layer. The fist layer is a input layer, the second layer is a competitive layer. Konen's learning rule is calculated distance between input data and weight, winner neuron that is the nearest neuron from learned weight can be a only output neuron. Only winner neuron and neighbor neuron of winner neuron can be adjusted through learning process. The distance between input vector and neuron can be expressed as follow equation.

$$d_j = \sum_{i=0}^{N-1} (X_i(t) - W_{ij}(t))^2 \qquad (5)$$

And the weight between neuron j and neighbor neuron is adjusted as followed equation. In previous equation, d_j is distance between neuron j and weight neuron.

And weight between neuron j and neighbor neuron can be readjusted as follow equation.

$$W_{ij}(t+1) = W_{ij}(t) + \alpha(X_i(t) - W_{ji}(t)) \qquad (6)$$

3. Design of Pattern Classifier for Defects

In this research, we was adapted backpropagation neural network that is a kind of multi-layer perceptron as the pattern classifier for defects in semiconductor package. That is a three –layer neural network including hidden layer between input layer and output layer. It takes a format as followed figure 6.
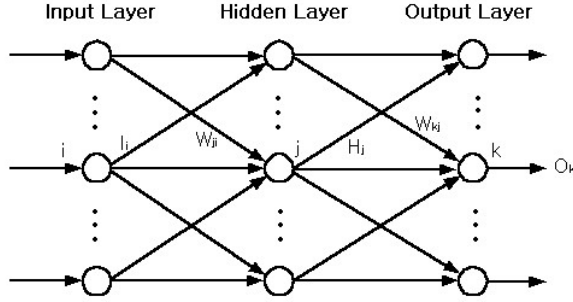

Fig.6 Backpropagation neural network

According to increment with number of hidden layer, in application to backpropagation neural network or multi-layer perceptron, the quality of decision boundary go on better. The case of 3-layer, we know what kind of decision boundary can be possible theoretically.

Fig.7 Decision boundary by number of layer

In this research, we adapted nonlinear function between hidden layer and output layer to sigmoid function that is formated to decision boundary with slow curve. Through this process, learning algorithm of backpropagation is performed. 3-layers including Input layer (I) and hidden layer (H) and output layer (O) are defined as followed eqoation for model of figure 6.

$$H_j = f(\sum_i W_{ji} \cdot I_i + \theta_j)$$
$$O_k = f(\sum_j W_{kj} \cdot H_j + \theta_k) \qquad (7)$$

For reducing mean squared error (E_p) between input layer (I) and hidden layer (H), weight(W_{ji}) can be adjustable as followed equation.

$$W_{ji} = -\eta_3 \cdot \frac{\delta E_p}{\delta W_{ji}} = \eta_3 \cdot \delta_j \cdot I_i \qquad (8)$$

Where, δ_j is output error, η_3 is learning rate of hidden layer.

For reducing mean squared error (E_p) between hidden layer (H) and output layer (O), weight(W_{kj}) can be adjustable as followed equation.

$$W_{kj} = -\alpha_2 \cdot \frac{\delta E_p}{\delta W_{kj}} = \eta_2 \cdot \delta_k \cdot H_k \qquad (9)$$

Mean squared error (E_t) can be expressed as followed equation for every pattern (P). Where,(T_{pk}) is target vector, (O_{pk}) is output vector.

$$E_t = \sum_p \sum_k (T_{pk} - O_{pk})^2/2 = \sum_p E_p \qquad (10)$$

Through these proceses, we can minimized error function (E_t) totally as reducing mean squared error (E_p) of each pattern P.

4. Inspection System and Test Algorithms

In this research, we was used SAT system including 3-axis scanner and ultrasonic transducer of 25MHz, SAT is made in HITACHI. Ultrasonic signal is converted image by software in SAT.

Photo.1 SAT system

And the software with test algorithms of semiconductor package are generated to m-code by Matlab5.3 made in Math Works. Test algorithms for defects in Semiconductor packege are expressed as followed figure 8. This test algorithms are composed of image process and self-organizing map as preprocess methods.
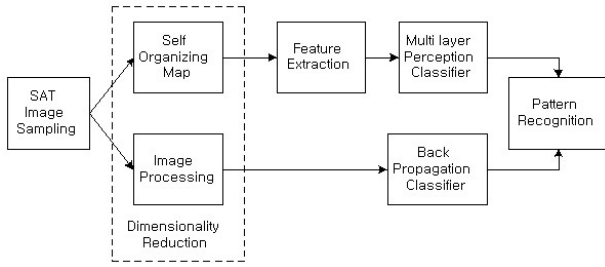
Fig.8 Test algorithm for semiconductor packege

Ultrasonic image acquired from SAT system is evaluated by user made software with test algorithm for semiconductor package, is displayed on monitor
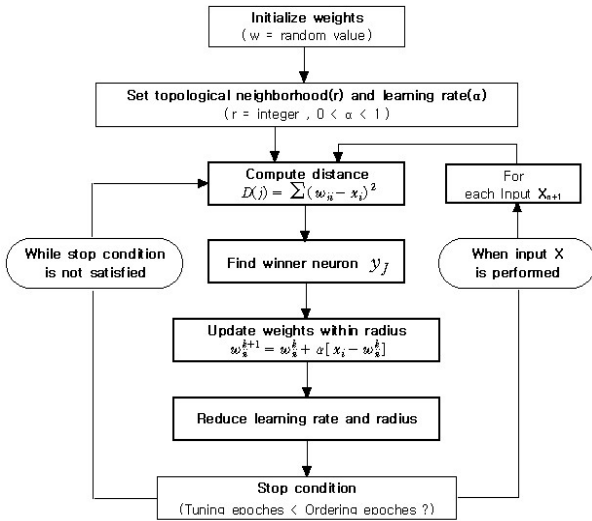

Fig.9 Algorithm for self-organizing map

Learning algorithm for self-organizing map is expressed as above figure 9. Learning Algorithm for backpropagation is presented as followed figure 10
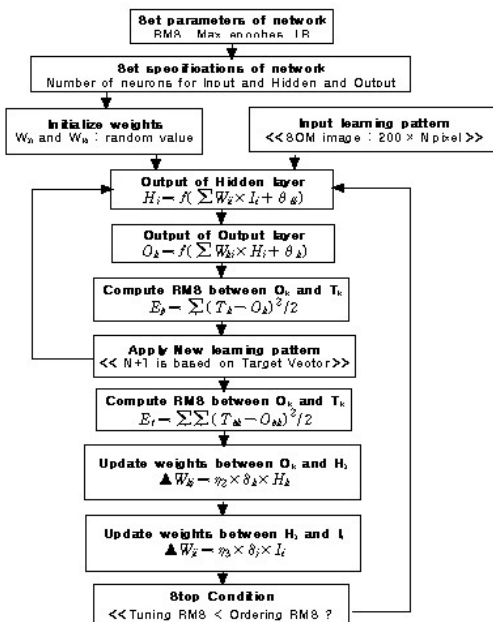

Fig.10 Algorithm for backpropagation network

Table.1 Test specimen

Type	Semiconductor Package	Defects
I815 (PBGA)		Delamination & Crack
I840 (PBGA)		Delamination
E0 (SBGA)		Crack

5. Experimental Results

5.1 Results of Image Preprocessing
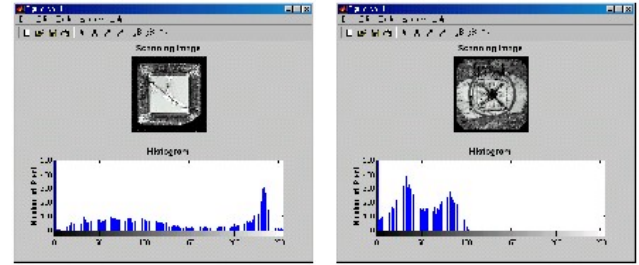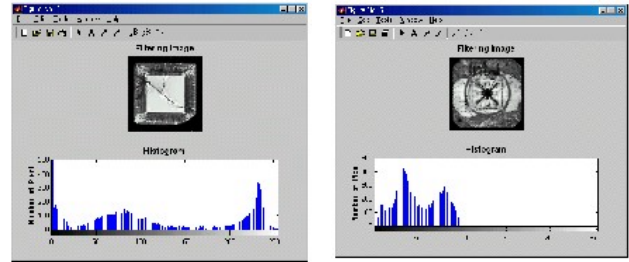

Fig.11 Scanned ultrasonic image
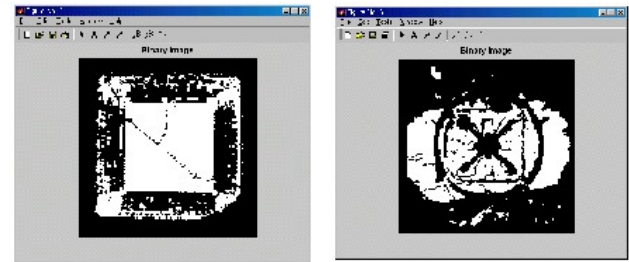

Fig.12 Equalization filtering image
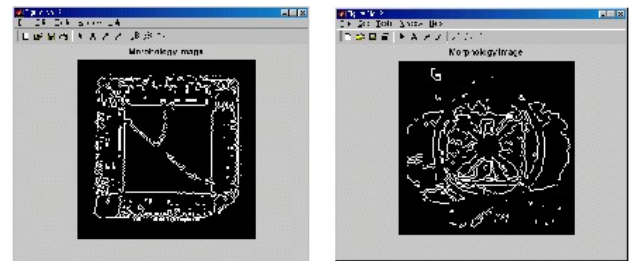

Fig.13 Binary image
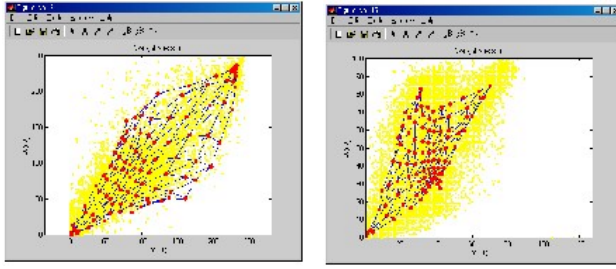

Fig.14 Edge detecting image

Fig.15 Self-organizing map

Through these preprocesses, input vector, that is inputed backpropagation neural network, is presented in figure 14 and figure 15. In figure 14, input data are number of 22,500, contents of data are composed of 0 and 1. And then we are able to reduce evaluation time of software for semiconductor package. In figure 13, input data are number of weights generating self-organizing map, are taken matrix with 10×10. contents of data are values between 0 and 255.

5.2 Reasults of Image Evaluating

In this research, preprocesses of dimensionality reduction are composed of image process and self-organizing map. We applied to backpropagation neural network, performed to evaluation for semiconductor package as applying backpropagation neural network to user made software.

a) E0

b) I840
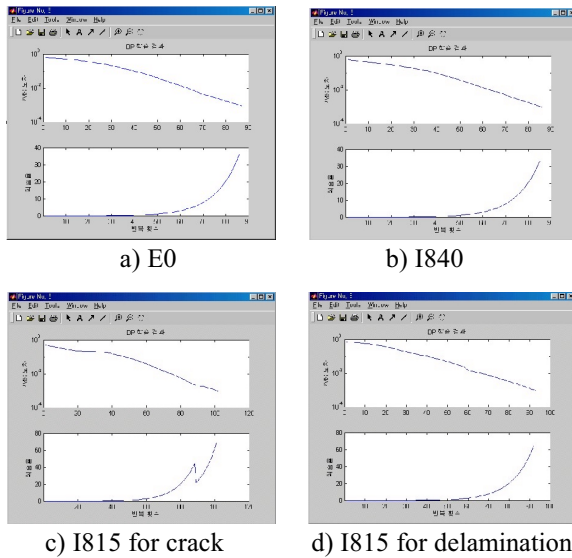

c) I815 for crack

d) I815 for delamination

Fig.16 Learning results for image processing

Learning results for self-organizing map is expressed as followed figure 17. Learning results for backpropagation network is presented as above figure 16.
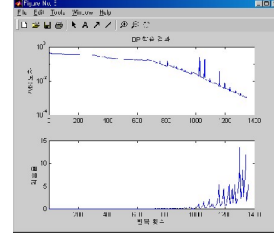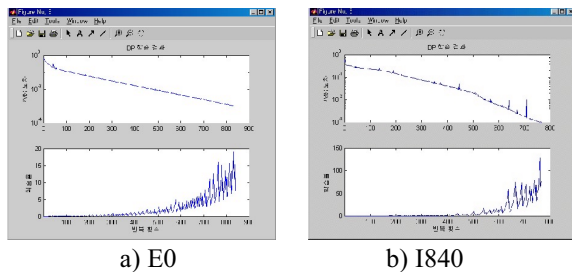

a) E0

b) I840

c) I815

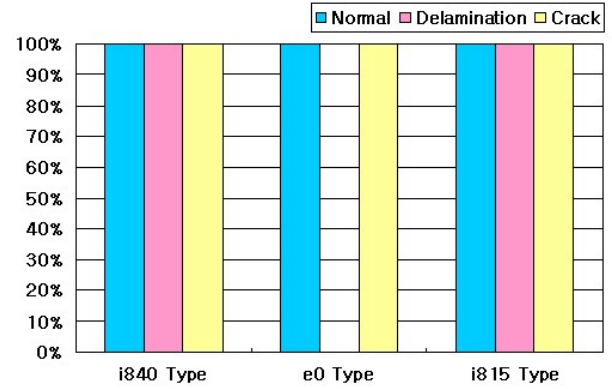Fig.17 Learning results for self-organizing map
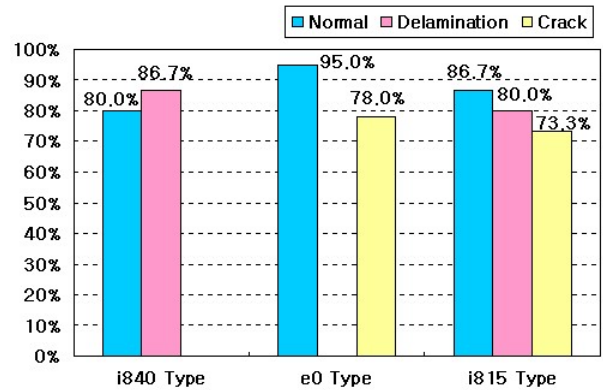

Fig.18 Test results for for image processing

Fig.19 Test results for for self-organizing map

The reason of results with 100% in figure 18 is due to apply various weights. We was able to increase classification rate of defects in semiconductor package by this reason. And the reason of results in self-organizing map is lower than image process can not taken results with 100% on structurally. For application industrial field, we was chosen test time and classification rate as important variables, was chosen the optimal condition was allowable.

Table.1 Test time in specimen

Image preprocessing	Test time	System specification
Image processing	≤ 03 sec.	CPU 700MHz
SOM (Self Organizing Map)	≤ 40 sec.	RAM 128MByte

Conclusions

Results, for adaptation of neural network and application of digital ultrasonic image processing, is followed.

1) We was obtained recognition rates of 83.4% and 75.7% for delamination and crack in application of self-organizing map as preprocess with dimensionality reduction.

2) We was obtained recognition rates of 100% in image processing with dimensionality reduction as application with various weights.

3) Test time was within 3 sec. in results of image processing, was within 40 sec. In results of self-organizing map.

References

1. A. Rosenfeld, A.C.Kak. "Digital Picture Processing." Academic Press, 1976.

2. H. Fukuoka·H. Toda. "Non-Destructive Stress Analysis by Acousticity." VDI-Berichte Nr. 313, pp. 245～687, 1978.

3. P. K. SAHOO.·S. DOLTANI. and A. K. C. WONG. "A Survey of Thresholding Techniques, Computer Vision, Graphics." AND IMAGE PROCESSING 41, pp. 223～250, 1988.

4. NOBUYUKI OTSU. "A Threshold Selection Method from Gray-Level Histograms." IEEE TRANSACTIONS ON SYSTEMS, MAN, AND CYBERNETICS, VOL. SMC-9, NO. 1, pp. 62～66, JANUARY 1979.

5. J. KITTLE.·J. ILLINGWORTH. "Minimum Error Thresholding, Pattern Recognition." Vol. 19, NO. 1, pp. 41～47, 1986.

6. ROBERT F. WANGER, STEPHEN W. SMITH, JOHN M. SANDRIK, and HECTOR LOPEZ. "Statics of Spekle in ultrasound B-Scans." IEEE TRANSACTIONS ON SONICS AND ULTRASONICS, VOL. 30, NO. 3, pp. 156～163, MAY 1983.

7. J. C. Lockwood et al. "High Speed method for Computing the exact solution for the pressure variations in the near field of a baffled piston." Journal of Acoustical Society of America, Vol. 53, pp. 735～739.

8. Gonzalez, R.C.. and Fittes, B.A.. "Gray-Level Transformations for Interactive Image Enhancement." Mechanism and Machine Theory, vol. 12, pp. 111～122, 1977.

9. Hall, E.L. et al. "A Survey of Preprocessing and Feature Extraction Techniques for Radiographic Image." IEEE Trans. Comput, vol. C-20, no. 9, pp. 1032～1044, 1971.

10. Hummel, R.A. "Histogram Modification Techniques." Technical Report TR-329, F-44620-72C-0062, Computer Science Center, University of Maryland, College Park, Md, 1974.

11. Woods, R. E. and Gonzalez, R. C.. "Real-Time Digital Image Enhancement." Proc. IEEE, vol. 69, no. 5, pp. 643～654, 1981.

12. Rosenfeld, A. and Kak, A. C.. "Digital Picture Processing." 2nd ed., Academic Press, NewYork, 1982.

13. Chaudhuri, B. B.. "A Note on Fast Algorithms for Spatial Domain Techniques in Image Processing." IEEE Trans. Syst. Man Cyb. , vol. SMC-13, no. 6, pp. 1166～119, 1983.

14. Huang, T. S. and Yang, G. T. and Tang, G. T. and Tang, G. Y.. "A Fast Two-Dimensional Median Filtering Algorithm." IEEE Trans. Acoust., Speech, Sig. Proc., vol. ASSp-27, pp. 13～18, 1979.

15. Pitas, I. and Vanetsanopoulos, A. N.. 'Nonlinear Digital Filters." Principles and Applications, Kluger, Boston, 1990.

16. Haralick, R. M. and Lee, J. S.. "Context Dependent Edge Detection and Evaluation." Pattern Recog., vol. 23, no. 1-2, pp. 1～20, 1990.

17. Sakison, D. J. and Algazi, V. R.. "Comparison of Line-by-Line and Two-Dimensional Encoding of Random Images." IEEE Trans. Pattern Anal. Machine Intell." vol. 12, no. 8, pp.814-817, 1971. IEEE Trans. Info. Theory, vol. IT-17, no. 4, pp.386～398.

18. Sakison, D. J. and Algazi, V. R.. "Comparison of Line-by-Line and Two-Dimensional Encoding of Random Images." IEEE Trans. Pattern Anal. Machine Intell." vol. 12, no. 8, pp.814-817, 1971. IEEE Trans. Info. Theory, vol. IT-17, no. 4, pp.386～398.

19. LAWRENCE A. HARRIS. "Element Directivity in Ultrasonic Imaging System." IEEE TRANSACTION ON SONICS AND ULTRASONICS, pp. 336～340, 1975.

20. H. L. Whaley and Las Adler. "Flaw Characterization By Ultrasonic Frequency Analysis." materials evaluation, pp. 182～192, 1971.

21. J. J. Hopfield. "Neural networks and physical systems with emergent collective computational abilities." Proc. Natl. Acad. Sci. USA, Vol. 79, pp. 2554～2558, 1982.

22. D. E. Rumelhart. and G. E. Hinton. and R. J. Williams. "Learning internal representations by error propagation." in Parallel Distributed Processing: Explorations in the Microstructure of Cognition. Vol. 1.: Foundations, D. E. Rumelhart. J. L. McClelland. and the PDP research group, Eds. Cambridge, Mass.: MIT Press, 1986, pp. 318～362.